

Andrea Arana

Structural concepts for metallic LH2 tank designs life enhancement

Faculty of Engineering and Applied Science

Aerospace Vehicle Design

MSc in Aerospace Vehicle Design

Academic Year: 2024-2025

Supervisor: Ioannis Giannopoulos

Date 25/08/2025



Faculty of Engineering and Applied Science
Aerospace Vehicle Design

MSc in Aerospace Vehicle Design

Academic Year: 2024-2025

Andrea Arana

Structural concepts for metallic LH2 tank designs life enhancement

Supervisor: Ioannis Giannopoulos
August 2025

This thesis is submitted in partial fulfilment of the requirements for the degree of MSc.
© Cranfield University 2025. All rights reserved. No part of this publication may be reproduced without permission.

Academic Integrity Declaration

I declare that:

- The thesis submitted has been written by me alone.
- The thesis submitted has not been previously submitted to this university or any other.
- All content, including primary and/or secondary data, is true to the best of my knowledge.
- All quotations and references have been duly acknowledged according to the requirements of academic research.

I understand that to knowingly submit work in violation of the above statement will be considered by examiners as academic misconduct.

Structural concepts for metallic LH2 tank designs life enhancement

Andrea Arana

Abstract

This thesis presents a fatigue analysis of preliminary designs for liquid hydrogen (LH_2) storage tanks manufactured from AA2219-T87 aluminium alloy with friction stir welded joints. A global finite element model (FEM) was developed to capture stress distributions under cryogenic conditions, supported by a refined submodel for accurate crack propagation analysis. Two approaches are examined: classical fatigue life estimation based on crack initiation using S–N data, and damage tolerance assessment through fracture mechanics of crack growth at cryogenic temperatures. Results indicate an overestimation of fatigue life during initiation, mainly due to assumptions and limited experimental evidence, while crack propagation is significantly faster and strongly influenced by environmental conditions and the thin tank walls. These findings highlight the importance of complementing structural-scale analyses with localised fracture assessments. Future work will focus on experimental validation and advanced monitoring techniques to improve the safety and reliability of LH_2 tanks.
Keywords: FEM, Crack, Fatigue, FSW, KI, Aluminium

NOMENCLATURE

AVD	Aerospace Vehicle Design
BM	Base Material
BWB	Blended Wing Body
CAD	Computer Aided Design
CFRP	Carbon Fiber Reinforced Polymers
CO_2	Carbon Dioxide
EV	Electric Vehicle
FEA	Finite Element Analysis
FEM	Finite Element Method
FSW	Friction Stir Weld
HAZ	Heat-Affected Zone
HE	Hydrogen Embrittlement
KI	Stress Intensity Factor
K_{IC}	Fracture Toughness (Mode I Critical Stress Intensity Factor)
LH_2	Liquid Hydrogen
MLI	Multi-Layer Insulation
NZ	Nugget Zone
SOFI	Spray-On Foam Insulation
TIG	Tungsten Inert Gas (welding)
TMAZ	Thermo-Mechanically Affected Zone
WNZ	Weld Nugget Zone
WT	Wing-Tube

Latin Symbol

a	Crack length [mm]
C	Paris law constant
E	Tank efficiency for ASME standard
g	Gravitational acceleration [m/s^2]
N	Number of cycles
P	Pressure [MPa]
p	Hydrostatic pressure [Pa]
R	Stress ratio
S	Allowable tensile stress [Pa]
t	Thickness [mm]
m	Paris law exponent

Greek Symbol

Δ	Difference or change; e.g. ΔK stress intensity factor range, ΔK_{th} threshold stress intensity factor range
ρ	Density [kg/m^3]
σ	Stress [Pa]

1.0 Introduction

1.1 Decarbonisation Efforts and Aviation Context

Climate change is a global challenge that affects every sector of society, requiring urgent action to reduce greenhouse gas emissions. One of the most critical indicators of this crisis is the record-high atmospheric carbon dioxide CO_2 concentration, which reached 422.45 parts per million (ppm) in 2024, the highest level ever recorded and a 52% increase over preindustrial values as illustrated in Fig. 1. This unprecedented increase is largely driven by fossil fuel combustion and land use changes, resulting in global total CO_2 emissions projected at 41.6 billion tons in 2024. The consequences of these emissions are profound, contributing to rising global temperatures, more frequent extreme weather events, and widespread ecological disruption[1].

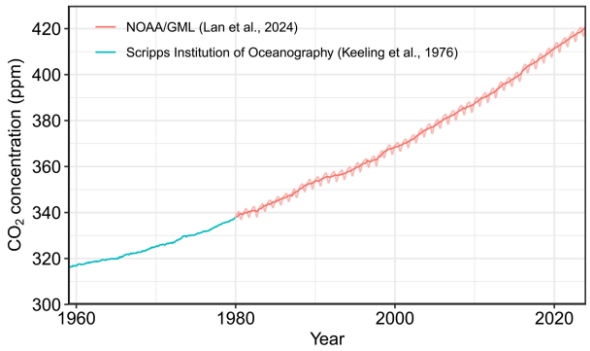


Figure 1: Surface Average Atmospheric CO_2 Concentration[1]

In response, various sectors are implementing major decarbonisation strategies. For example, the automotive industry is rapidly adopting electrification, with electric vehicles (EVs) and hybrid technologies replacing traditional internal combustion engines. This transition is supported by advances in battery technology, charging infrastructure, and supportive policy frameworks, all aimed at reducing the sector's carbon footprint[2].

Aviation, while accounting for a smaller share of total emissions, plays a significant role in climate change. In 2024, aviation was responsible for 2.5% of global CO_2 emissions, a figure that has remained relatively stable in recent years despite improvements in aircraft efficiency. When considering non-CO_2 effects such as contrails and nitrogen oxides, aviation's overall contribution to global warming is even higher, estimated at around 4%. For context, direct emissions from aviation accounted for 3.8% to 4% of total greenhouse gas emissions in the European Union in 2022[3].

Aviation is pursuing sustainability through electrified propulsion, using electric motors powered by batteries, fuel cells, or hybrids to reduce fossil fuel dependence. Advances have enabled electric systems for small planes and urban air mobility, while hybrid-electric designs for short-haul flights promise lower emissions and fuel use. Yet, limited battery energy density prevents wide adoption for longer routes, revealing the need for alternative, higher-density, low-emission solutions beyond current electrification technologies[4].

Hydrogen in Aviation: Opportunities and Challenges

Hydrogen has emerged as a highly promising candidate for the decarbonisation of aviation. As an energy carrier, hydrogen offers several key advantages: it produces zero CO_2 emissions at the point of use and has a high specific energy of about 120 MJ/kg compared to 43 MJ/kg for conventional jet fuel , approximately three times that of conventional jet fuel by mass. When produced using renewable energy sources, its entire lifecycle emissions can be near zero. However, hydrogen's volumetric energy density is significantly lower at approximately 8.5 MJ/L compared to 35 MJ/L for kerosene, requiring storage tanks approximately four times larger by volume for the same energy content[5].

In aviation, hydrogen can be utilized in two main ways: (i) hydrogen combustion, in which it is burned in modified gas turbines, producing only water vapor as a by-product with minimal nitrogen oxide emissions; and (ii) hydrogen fuel cells, which convert hydrogen directly into electricity to power electric motors, providing a highly efficient and emission-free propulsion method[4].

Major aerospace manufacturers and research institutions are investing heavily in hydrogen technologies to accelerate the decarbonisation of aviation. One of the leading examples is Airbus, which launched its ZEROe project in 2020 with the ambition to develop the world's first hydrogen-powered commercial aircraft by 2035[6].

Following extensive research into both hydrogen combustion and fuel cell technologies, Airbus announced in 2025 that fuel cell technology had been selected as the propulsion method for future aircraft, featuring four 2-megawatt electric propulsion engines powered by hydrogen fuel cells. However, recent industry reports[7] indicate that commercial introduction timelines may extend 5-10 years beyond the original 2035 target, highlighting the complexity of the engineering challenges involved. In addition, companies like ZeroAvia have made significant progress in demonstrating hydrogen-powered flight. ZeroAvia has successfully completed a series of test flights with its Dornier 228 aircraft, equipped with a hydrogen-electric powertrain[8].



a) Airbus ZeroE BWB Concept
(Airbus image)



b) ZeroAvia Dornier 228 Test Aircraft
(ZeroAvia image)

Figure 2: Illustrative Examples of Ongoing Developments in Hydrogen-Powered Aviation

These milestones reflect the growing momentum and commitment within the aerospace sector to make hydrogen-powered, zero-emission flight a commercial reality in the coming decade. However, the storage and handling of liquid hydrogen on board aircraft present significant engineering challenges, as it requires maintaining cryogenic temperatures. Furthermore, hydrogen's low volumetric density necessitates much larger tanks than those for conventional fuels, complicating structural integration and influencing weight distribution, centre of gravity, and overall aircraft performance. This marks a period of innovation for the field of aviation engineering.

1.2 Objectives and Scope of the Thesis

The primary objective of this thesis is to establish a structural design for a metallic tank optimised for the storage of liquid hydrogen in aviation applications, with particular emphasis on crack propagation to ensure that the tank meets operational requirements. To achieve this objective, the thesis is structured around several interrelated aims.

The first phase involves the preliminary design, synthesising insights from recent studies and established literature, including established equations, in order to define the optimal tank geometry, material selection, manufacturing processes, insulation strategies, and attachment methods for integration within the aircraft fuselage.

Following the preliminary design, an analytical design phase and finite element analysis (FEA) will be conducted under representative operational load cases. These simulations enable a robust comparison between analytically derived and numerically obtained stress distributions, thereby identifying the maximum loading conditions experienced by the tank. This combined analytical–numerical approach both validates and cross-checks the underlying design assumptions.

A detailed fracture mechanics investigation will be undertaken on the critical regions of the tank. In particular, finite element method (FEM) analyses will be performed to evaluate the stress intensity factor (K_I) as a function of crack size, thereby providing a basis for assessing fracture risk under operational conditions. Particular attention will be devoted to the weld region, which is recognised as a probable site for crack initiation and propagation due to microstructural alterations induced by welding.

Building upon the crack characterisation, the next stage will estimate the tank's fatigue life under representative cyclic loading typical of aviation service. This will apply Paris' Law methodologies, with particular emphasis on how cryogenic temperatures affect crack propagation rates in the various weld zones.

Finally, the tank design will be validated by assessing compliance with established safety margins. Should the design prove inadequate, alternative design or attachment solutions will be proposed and evaluated accordingly.

It should be clearly stated that, due to practical limitations in budget, time, and the complexity of experimental testing in cryogenic environments, this thesis will rely exclusively on secondary data obtained from journal literature and authoritative technical references. Consequently, the study will necessarily involve a series of explicit assumptions, which will be clearly identified and justified throughout the thesis.

2.0 Literture Review

2.1 Hydrogen Tank Configuration

2.1.1 Fundamental Properties and Storage Challenges

While liquid hydrogen offers a high specific energy by mass, its very low volumetric energy density requires significantly larger storage tanks, about four times the volume of kerosene tanks for the same energy content. This volumetric constraint remains the main challenge for aircraft integration, impacting aerodynamics, structural design, and weight[9]. Additionally, LH_2 must be stored at extremely low temperatures (below $-253°C$) and has a low density of around 70 kg/m^3, as illustrated in Fig. 3, while gaseous hydrogen at standard temperature and pressure is even less dense at approximately 0.0899 kg/m^3, both of which contribute to significant volumetric storage challenges. For aviation, liquid hydrogen is preferable over gaseous hydrogen because gaseous hydrogen must be stored at very high pressures, requiring much heavier and more robust tank structures that dramatically increase overall aircraft weight[10].

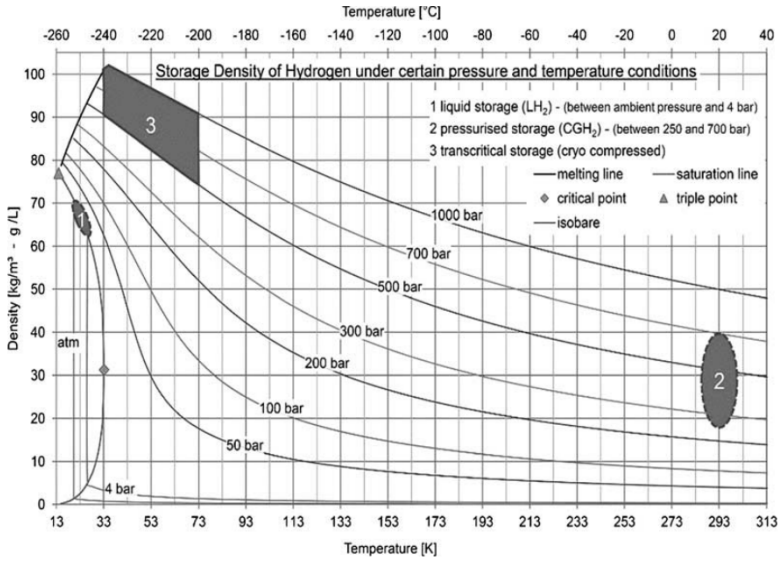


Figure 3: Hydrogen storage density under different pressure and temperature conditions[11]

The cryogenic nature of liquid hydrogen causes continuous boil-off as environmental heat vaporises the fuel, leading to pressure build-up that must be vented to avoid over-pressurisation. This results in fuel loss and operational challenges, especially during extended ground or dormancy periods[12,13]. Research shows boil-off rates decrease with larger tank sizes due to lower surface area-to-volume ratios, while smaller tanks suffer proportionally higher heat ingress and losses[4].

2.1.2 Tank Design and Integration Strategies

Contemporary research has identified several approaches to integrating liquid hydrogen storage systems within aircraft configurations. Non-integral tank designs offer flexibility in placement and maintenance access but require additional structural supports and may result in suboptimal volumetric efficiency. Conversely, integral tank concepts maximise space utilisation by incorporating the tank structure as part of the aircraft's primary load-bearing framework, though this approach presents challenges for maintenance and system accessibility[9,14].

Geometric optimisation demonstrates that cylindrical tank configurations with domed end caps represent the most practical compromise between manufacturing feasibility and thermal efficiency. While spherical geometries would theoretically minimise surface area-to-volume ratios and reduce heat ingress, their integration within conventional aircraft configurations presents significant challenges[15,16]. Recent conceptual studies have explored alternative aircraft configurations, including BWB (Blended Wing-Body) designs and distributed propulsion systems, specifically to accommodate the volumetric requirements of liquid hydrogen storage more effectively, as well as tank integration into current (WT) wing-tube aircraft configurations to optimise structural efficiency and maintain aerodynamic performance Fig. 4[17,18].

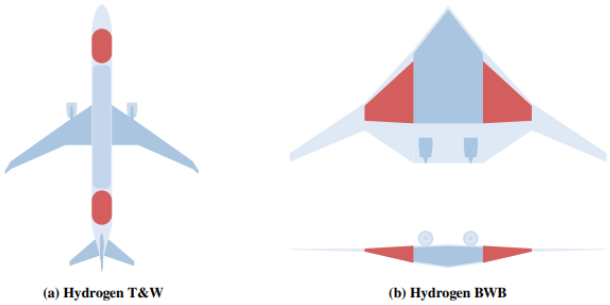


Figure 4: Hydrogen storage concepts for aviation[18]

2.1.3 Material Selection and Structural Considerations

Aluminum alloys, particularly AA2219, have emerged as the preferred material for liquid hydrogen tank construction due to their excellent strength-to-weight ratio, proven cryogenic performance, and resistance to hydrogen embrittlement[19]. These materials maintain structural integrity at cryogenic temperatures while exhibiting minimal susceptibility to hydrogen-induced degradation that affects many high-strength steels.

Austenitic stainless steels, including grades 304 and 316, provide alternative solutions with superior hydrogen compatibility but at the cost of increased weight[20,21]. Advanced composites like carbon fibre reinforced polymers (CFRP) provide significant weight savings but face challenges with hydrogen permeability and microcracking from thermal cycling. Recent advances in thin-ply composites and thermoplastic matrices show improved damage tolerance and resistance to cryogenic cycling[22]. These promising developments suggest composite tanks may be viable in the future, though technology readiness levels still need to improve for certification.

2.1.4 Insulation Technologies and Thermal Management

Effective thermal insulation is critical for minimising boil-off losses and maintaining operational efficiency. Multi-layer insulation (MLI) systems provide the highest thermal performance, achieving effective thermal conductivities as low as $0.135 mW/m - K$ under high vacuum conditions[23]. However, MLI systems require complex double-wall construction with vacuum maintenance systems, adding significant weight and complexity to the overall storage system.[24,25]. Boil-off occurs not only during ground storage but also continuously during flight and refueling operations, necessitating careful management to prevent fuel loss and maintain tank pressure within safe limits[12]. Spray-on foam insulation (SOFI) offers a simpler, lighter alternative but has lower thermal performance and degrades under thermal cycling. Advanced closed-cell polyurethane foams have shown promise in aerospace, though long-term durability under repeated cryogenic cycles is still being studied[25,26].

2.1.5 Manufacturing Technologies and Processes

The fabrication process involves metal forming techniques to create fine-grained or nanocrystalline aluminum alloys that improve hydrogen trapping and resist embrittlement. Controlled milling optimises particle and grain sizes for better hydrogen absorption and release, while microstructural advances such as dual-precipitate alloys enhance strength and durability[27].

For the cylindrical parts of the tanks, backward extrusion is a common method due to its ability to produce seamless, high-integrity structures with excellent mechanical properties[28]. In contrast, the domes are typically formed using hydroforming or spinning processes, which allow for precise shaping and thinning of the material while preserving strength and ductility[29,30]. These combined manufacturing approaches ensure the structural reliability and performance necessary for demanding cryogenic hydrogen storage applications.

The joint between the domes and the cylindrical section in aluminum hydrogen storage tanks is typically achieved using friction stir welding (FSW), a solid-state joining process that has demonstrated superior performance compared to traditional fusion welding methods. FSW employs a rotating tool that generates frictional heat to soften, but not melt, the material, allowing plastic deformation and mixing of the metal at the joint interface. This process yields welds with mechanical efficiencies ranging from 70% to nearly 100%, while effectively eliminating common defects such as porosity, cracking, and heat-affected zone degradation. The resulting welds are fully sealed, structurally robust, and capable of maintaining integrity under the demanding pressure and temperature conditions characteristic of hydrogen storage[28,31].

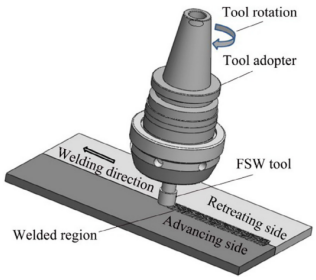


Figure 5: Schematic Diagram of Friction Stir Welding Process[32]

2.1.6 Safety Analysis and Load Case Considerations

Liquid hydrogen storage systems must withstand a complex array of operational and emergency loading conditions while maintaining structural integrity and performance. Primary load cases include internal pressurisation (typically 1-1.5 bar operational pressure), hydrostatic loads from fuel sloshing during flight manoeuvers, and thermal stresses from cryogenic temperature differentials[33,34]. Aircraft-level loading conditions, including ultimate loads of 9g and crash scenarios, must be accommodated without compromising tank integrity[35,3].

Hydrogen-specific hazards present unique challenges requiring specialised safety measures. Hydrogen's wide flammability range (4-75% in air) and extremely low ignition energy create significant fire and explosion risks that must be addressed through comprehensive leak detection, ventilation, and ignition source control. Hydrogen embrittlement effects on structural materials require careful material selection and long-term surveillance programs to ensure continued structural integrity. Pressure relief systems must be designed for the specific characteristics of hydrogen service, including rapid pressure rise rates and the potential for invisible hydrogen flames[36,37].

2.2 Fatigue in Cryogenic Environment

2.2.1 Classical Fatigue and Damage Tolerance Approaches

Fatigue damage in metallic structures is traditionally understood as a progressive process that ultimately leads to failure under cyclic loading. The classical fatigue approach divides the fatigue life into two distinct phases: crack initiation and crack propagation. The crack initiation phase refers to the period during which microstructural damage accumulates without the presence of a macroscopically detectable crack. This phase can represent a significant portion of the total fatigue life, often estimated to range between 70% and 90% for various metallic alloys and welded joints[38]. Classical fatigue analysis relies heavily on stress-life (S-N) curves, which correlate cyclic stress amplitude to the number of cycles leading to failure. The Miner's linear damage rule is commonly applied to account for variable amplitude loading, enabling a cumulative damage calculation from different stress levels[39].

Within this traditional framework, the integrity of the structure is assumed intact during the initiation phase, with no pre-existing flaws that compromise its load-carrying capacity. This assumption is valid for many engineering applications where careful manufacturing and inspection processes minimise initial defects. However, the microstructural nature of fatigue damage means that crack initiation can be difficult to detect and predict precisely, especially in complex welded joints and harsh environments.

In contrast, the damage tolerance methodology adopts a more conservative and realistic premise. Damage tolerance assumes the presence of small cracks or manufacturing defects from the outset and focuses on predicting the rate of crack growth under cyclic stresses. This approach utilises fracture mechanics principles and experimentally derived crack growth laws, such as Paris' law, to estimate the remaining service life based on the propagation of these flaws to a critical size. Damage tolerance thus emphasises inspection, monitoring, and maintenance to detect and manage cracks before they reach a critical length that could cause catastrophic failure[39].

At the academic level, integrating classical fatigue approaches with damage tolerance methodology is essential for a more comprehensive and profound understanding of structural behaviour under cyclic loading. While classical fatigue studies focus on the time to crack initiation, damage tolerance provides the perspective of crack growth and propagation, emphasising structural integrity in the presence of defects. Therefore, this complementary approach strengthens learning, supports applied research, and provides a better understanding of fatigue life.

2.2.2 Crack initiation and propagation under Cryogenic Temperatures

When considering fatigue crack initiation mechanisms at cryogenic temperatures near 20 K, materials such as the 2219-T87 aluminum alloy exhibit altered mechanical responses that influence fatigue behaviour. Specifically, tensile testing reveals a significant increase in yield strength and ultimate tensile strength at cryogenic temperatures compared to room temperature (Fig. 6), while the material retains adequate toughness. This increase in strength may affect the initiation and early propagation stages of fatigue cracks by modifying the local stress and strain fields around defects, underscoring the importance of understanding fatigue mechanisms in cryogenic environments for aerospace structural applications [19,40].

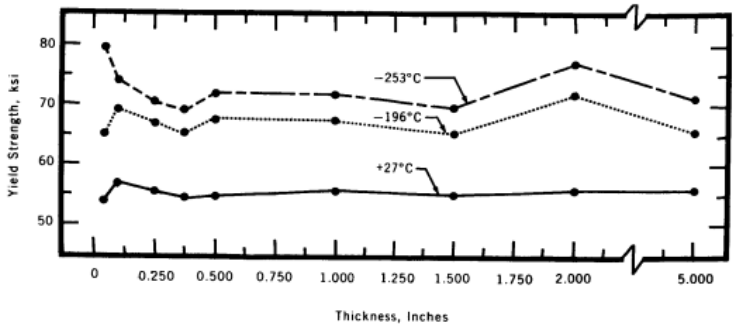


Figure 6: Low Temperature Yield Strength of A2219-T87 [40]

Importantly, the fatigue crack growth threshold (ΔK_{th}) increases by approximately 20–30% at 20 K relative to ambient conditions, reflecting enhanced resistance to crack initiation under cyclic loading at cryogenic temperatures. This improvement in the threshold intensity factor significantly contributes to the alloy's durability in low-temperature service environments [19,41].

In conventional service environments, the Paris Law parameters C and m are regarded as material-dependent constants that remain relatively stable within a given microstructure. These parameters facilitate the prediction of fatigue crack growth rates as a power-law function of the stress intensity factor range (ΔK), thus forming a cornerstone of structural life prediction models [39]. However, under cryogenic conditions, shifts in microstructural behaviour and fracture mechanics induce significant variations in these parameters. Changes in dislocation mobility, crack tip plasticity, and other low-temperature-specific mechanical phenomena alter both C and m, as well as the threshold ΔK_{th} [19,42].

Specifically for aluminium alloys, the Paris exponent m typically falls between 3.5 and 4 and remains relatively stable despite temperature variations. Conversely, the Paris constant C demonstrates appreciable sensitivity to temperature, decreasing at cryogenic temperatures around 28% for 6061-T62[43], which corresponds to reduced fatigue crack growth rates for a given ΔK. The accompanying increase in fatigue thresholds reinforces resistance to both crack initiation and propagation at low temperatures. This behaviour aligns with analogous observations in a variety of metallic systems, where lower temperatures elevate threshold stress intensity ranges and suppress crack growth rates, thereby reducing C without markedly affecting m[39,19].

Overall, these temperature-dependent variations in Paris Law parameters underscore the critical need for fatigue life models to incorporate environmental and temperature influences, particularly when predicting the performance of aerospace structural materials such as 2219-T87 aluminum alloy operating in cryogenic settings.

2.2.3 Hydrogen Embrittlement

Hydrogen embrittlement (HE) is a degradation process in which metals lose ductility and fracture toughness due to the absorption of atomic hydrogen, potentially leading to catastrophic failure often without visible warning[44]. Atomic hydrogen permeates metallic structures through several pathways, including corrosion reactions, direct exposure to high-pressure hydrogen atmospheres in storage tanks and pipelines, and manufacturing processes such as welding or forging[45]. Once absorbed, hydrogen atoms diffuse through the metal's crystal lattice and preferentially accumulate at microstructural trapping sites such as dislocations, grain boundaries, and precipitates. This diffusion is accelerated by stress gradients, especially in regions with high triaxial stress, which concentrate hydrogen at vulnerable sites and promote embrittlement mechanisms. The severity of HE depends on factors including material composition, hydrogen concentration, applied stress, and environmental conditions[46]. In hydrogen storage and transport systems, these processes lead to subcritical crack growth and mechanical weakening, posing a significant reliability risk[45,47].

Hydrogen embrittlement significantly degrades mechanical properties, especially ductility, causing commercial aluminum alloys to lose up to 40% of elongation and reduction in area, with a shift from ductile to brittle fracture modes[48]. Although aluminum alloys generally resist embrittlement better than steels, some high-strength variants remain vulnerable[49]. The AA2219 alloy in T87 temper shows relatively low susceptibility due to its moderate strength compared to more embrittlement-prone 7xxx-series alloys[50,51]. Yield strength is mostly unaffected, but sudden failures below yield stress can occur due to localised mechanisms[44], posing critical risks for hydrogen-exposed components like storage tanks[47].

Hydrogen penetrates metallic structures in both gaseous and aqueous forms, diffusing through microstructural defects such as dislocations, vacancies, inclusions, and grain boundaries. Once absorbed, hydrogen exists in atomic, molecular, or mixed states, promoting localised stress concentration that leads to crack nucleation and propagation. These fracture processes can initiate even under stresses below the material's yield strength, as hydrogen-induced defects serve as critical weakening sites, causing catastrophic brittle failures[44].

2.2.4 Crack propagation in FSW joints

FSW is widely regarded as one of the most reliable solid-state joining technologies, enabling the fabrication of joints with excellent mechanical performance in alloys traditionally considered difficult to weld by fusion techniques[52]. For this reason, it has been broadly applied in critical sectors such as aerospace, automotive, and hydrogen storage. Despite these advantages, maintaining structural integrity remains a key challenge, since even microscopic flaws can act as precursors of failure through crack initiation and propagation[53].

The weld microstructure generated by FSW is highly heterogeneous, shaped by the complex thermal and mechanical cycles of the process. The nucleation zone (NZ) undergoes substantial plastic deformation at elevated but sub-solidus temperatures, leading to dynamic recrystallisation and the formation of fine grains. This grain refinement enhances ductility and fracture toughness but may reduce hardness due to precipitate dissolution, especially in precipitation-strengthened alloys[54]. Adjacent to it, the thermomechanically affected zone (TMAZ) experiences both strain and temperature but lacks complete recrystallisation, resulting in elongated grains and reduced hardness due to precipitate coarsening. Finally, heat affected zone (HAZ) is influenced solely by the thermal cycle, where over-aging and precipitate coarsening lead to the lowest hardness and strength within the weld[55]. These differences explain why fracture and fatigue failures often localise in the TMAZ and HAZ, which consistently act as the weakest links in the welded joint.

The fatigue and fracture behavior of FSW joints is therefore controlled by this microstructural heterogeneity. Cracks frequently initiate in the softened HAZ or TMAZ, although they may also nucleate at local stress concentrators such as voids, inclusions, or surface irregularities left by the tool shoulder[56,57]. After initiation, propagation follows the path of least resistance. The highly refined and ductile SZ may facilitate relatively fast crack growth under cyclic loading, while propagation through the TMAZ and HAZ can be slower and more tortuous due to plastic incompatibility and residual stress effects[58,59]. Experimental studies have shown that the threshold stress intensity and crack growth constants vary significantly among the SZ, TMAZ, and base material, indicating that microstructural zones alter both initiation resistance and growth kinetics (Fig. 7).

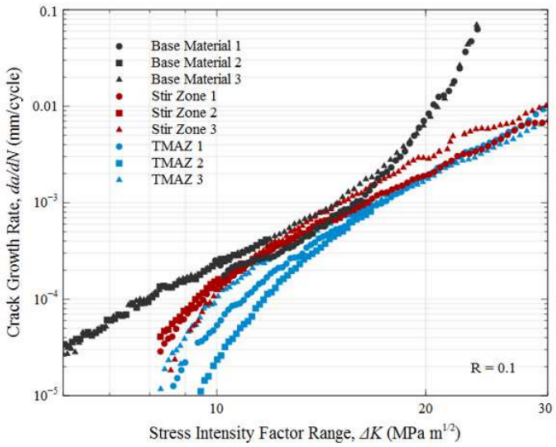


Figure 7: Fatigue crack growth data for base material, TMAZ, and stir zone samples[59]

3.0 Methodology

This study adopted a sequential engineering design and analysis methodology, beginning with a comprehensive literature review to establish the theoretical framework and guide the preliminary configuration of the tank. The initial phase encompassed decisions regarding geometry, integration with and attachment to the fuselage, material selection, and thermal insulation. Structural performance was subsequently assessed through a two-stage FEM approach: first, a global model was developed to evaluate overall structural behaviour, followed by a detailed submodel focusing on critical regions. Stress data obtained from the submodel was then used in a fracture mechanics analysis to estimate crack propagation cycles and predict fatigue life. The resulting findings enabled the identification of fatigue-critical areas, provided an evaluation of structural durability, and supported the proposal of design improvements aimed at future optimisation.

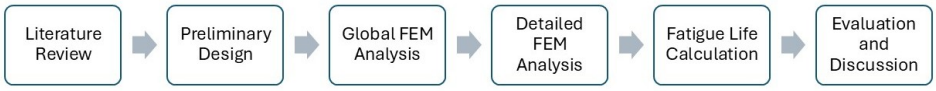


Figure 8: Flowchart illustrating the key phases of the project methodology

3.1 Preliminary design

During the preliminary design phase, a comprehensive comparative assessment was conducted, encompassing material selection, manufacturing feasibility, integration strategies, and insulation concepts, grounded in findings from relevant aerospace literature. To this end, several decision matrices were developed to evaluate the possible alternatives, the details of which are provided in Appendix B, thereby enabling a systematic comparison of design options. The outcome of this multi-criteria evaluation, as summarised in Table 1, facilitated the identification of the optimal configuration for the intended application.

Table 1: Overview of Preliminary Design Selections

Feature	Design Decision
Tank Material	Aluminum Alloy AA2219-T87
Integration	Non-integral, bolted frames
Insulation	MLI
Manufacturing	Cylindrical: Deep drawing, Domes: Hydroforming, Joints: Friction Stir Welding (FSW)

Based on these design decisions, the tank dimensions were established according to constraints imposed by the fuselage envelope and informed by the selected parameters. For the design, it will be assumed that the tank is integrated into an A320 fuselage, which sets the constraints for design parameters and informs other requirements. The maximum tank diameter is limited to 3 meters, constrained by the A320 fuselage diameter to ensure proper clearance and structural compatibility[60]. Following the literature, a diameter-to-length ratio of approximately 0.66[61] was adopted to define the tank length accordingly.

Furthermore, an analysis of the impacts on aircraft range and passenger capacity was conducted, as detailed in Appendix C, comparing hydrogen tank integration with conventional kerosene-fueled configurations. The results of this analysis are presented in Table 2.

Table 2: Key Dimensions and Capacities of the Hydrogen Tank

Feature	Value	Units
Length	5000	mm
Volume	28.27 (60% of A320)	m^3
Range	1879	km
Passengers	126	u

3.1.1 Minimum Thickness Calculation

Based on internal pressurisation as the governing load case, the minimum required thickness of the tank wall is calculated following the formulation prescribed by pressure vessel design codes[62]. This approach refines the classical thin-walled pressure vessel equation by incorporating factors such as the material allowable stress, joint efficiency, and an accounting term for pressure correction, ensuring compliance with safety and operational standards.

The governing equation for minimum thickness is:

$$t_{\text{min}} = \frac{P \cdot r}{S \cdot E - 0.6 \cdot P} \quad \text{(62)} \tag{1}$$

Where:

- P is the design internal pressure, accounting for safety factors,
- r is the internal radius of the tank,
- S is the allowable tensile working stress of the material at operating temperature,
- E is the joint efficiency factor related to the quality of welds and inspections.

For liquid hydrogen tanks in aircraft, typical operational pressures range between 1 and 1.5 bar absolute. However, transient scenarios such as venting or rapid temperature fluctuations can temporarily increase this pressure beyond nominal levels. To conservatively account for these eventualities and ensure structural safety, an ultimate safety factor of 3 is applied in accordance with CS25 standards[3] for low-pressure vessels. This results in a design pressure given by:

$$P_{\text{design}} = 1.5 \text{ bar} \times 3 = 4.5 \text{ bar} = 0.45 \text{ MPa} \tag{2}$$

The material selected for the tank (A2219-T87) exhibits a yield strength of approximately 393 MPa (57 ksi) at room temperature (27°C) (Fig. 6). To address uncertainties such as hydrogen embrittlement, a reduction factor of 0.8 is applied to the allowable material strength, as recommended in the literature regarding hydrogen service and material performance factors[19].

Additionally, a conservative safety factor of 1.15 is applied to the material strength, leading to a design allowable tensile stress of approximately:

$$\sigma_p = \frac{0.8 \times 393 \text{ MPa}}{1.15} \approx 341.8 \text{ MPa} \tag{3}$$

As studies have shown, Friction Stir Welding of aluminum alloys such as AA2219 yields welds with mechanical efficiencies ranging from approximately 70% to nearly 100% depending on welding parameters and process control[28]. The microstructural refinement and reduced defects compared to fusion welding translate into joint efficiencies typically in the range of 0.85 to 0.95[63].

Considering the rigorous inspection and qualification standards in aerospace manufacturing, an initial joint efficiency value of E=0.85 is assumed for this study as a conservative yet realistic parameter for structural calculations.

Applying the calculated values to Equation (1):

$$t_{\text{min}} = \frac{0.45 \text{ MPa} \times 1500 \text{ mm}}{341.8 \text{ MPa} \times 0.85 - 0.6 \times 0.45 \text{ MPa}} \approx \frac{675}{290.53 - 0.27} = \frac{675}{290.26} \approx 2.33 \text{ mm} \tag{4}$$

This theoretical minimum thickness is increased to a conservative initial wall thickness of 3.5 mm. This choice accounts for uncertainties in manufacturing tolerances, extended operational loads, and the inactive safety margins commonly adopted in aerospace cryogenic storage designs. Additionally, the decision was informed by comparisons with similar designs in previous projects[35,64,65], which support the selected thickness as both safe and practical.

With a wall thickness of 3.5 mm, the hoop stress under internal pressurisation is approximately 192 MPa, which aligns with standard aerospace practice for cryogenic hydrogen storage and provides an additional safety margin to manage material behaviour uncertainties and load variations. Since experimental validation lies outside the scope of this thesis, this conservative thickness serves as a robust initial baseline for the subsequent detailed structural verification via finite element analysis.

3.2 Load Cases Definition

The structural verification of the liquid hydrogen (LH_2) storage tank requires consideration of the full spectrum of mechanical solicitations expected during a 25-year service life. In accordance with the methodology[66], a representative envelope of load types has been defined, encompassing both operational cycles and certification-driven extremes. Table 3 summarises these load categories in terms of cycle frequency, stress variation, and stress ratio.

Table 3: Loading Types for LH_2 Storage Tanks in Regional Aviation[66]

Loading Type	Cycle Frequency	Stress Variation	Stress Ratio (R)
Storage pressurisation	Low	Large	0
Pressure control system	High	Small	0.9
Ground manoeuvring and gusts	High	Small–medium	0.2
Extreme manoeuvring	Very low	Very large	0

Cycle Quantification within the Operational Envelope

In all cases, to ensure the structural integrity of the component throughout its service life, a conservative approach is adopted by considering the most critical scenario within the operational envelope. This means that the maximum number of cycles and the most severe stress ratio R are assumed for each load case, ensuring that the design accounts for the highest possible fatigue demand.

Pressurisation cycles ($R = 0$) correspond to refills from ambient pressure to 1.5 bar prior to flight. For a regional aircraft operating three sectors daily without fuel tankering, two full refills per day are assumed, leading to:

$$2 \times 365 \times 25 = 18,250 \text{ cycles}.$$

Valve venting due to thermal boil-off and ambient pressure variations occurs intermittently during flight. Literature reports a typical frequency of one to two events per day[67,68], yielding:

$$2 \times 3 \times 365 \times 25 \approx 54,750 \text{ cycles},$$

with $R \approx 0.9$ given the narrow stress fluctuation.

Gust and manoeuvre responses contribute additional stress variations in the range $R = 0.2$–0.3. Assuming 3–5 significant events per sector[69], one obtains:

$$5 \times 3 \times 365 \times 25 \approx 136,875 \text{ cycles}.$$

Finally, extreme manoeuvres under combined inertial loads ($R = 0$) are rare, expected once or twice over the lifetime of the airframe[70]. These scenarios, although exceptional, are prescribed by certification frameworks such as CS-25[3] and must be considered for ultimate load verification.

Selection of Load Cases for Analysis

Although three principal load cases were modelled in detail using finite element methods, additional operational loads were accounted for using simplified analytical calculations, literature data, and conservative scaling based on FEM results. This hybrid approach allowed the incorporation of service condition variability while remaining computationally manageable. Using Miner's rule to accumulate fatigue damage, both detailed and estimated stress cycles were integrated to provide a comprehensive prediction of the component's fatigue life.

Baseline pressurisation

The reference load case consists of steady internal tank pressurisation, representing the nominal operating condition across all flight altitudes. Variations due to the pressure control system are conservatively modelled as 1.1 times the nominal stress.

Pressurisation with severe inertial loads

These cases assess the interaction of internal pressure with inertial accelerations representative of realistic manoeuvres. The loads examined correspond to 2.5g vertical, 1.5g longitudinal, and 3g lateral, combined individually with nominal pressurisation. This approach parallels CS-25 certification practice[(3)], where pressurisation and inertia may be applied in combination.

Pressurisation with extreme inertial envelopes

Selected ultimate load scenarios are included to verify robustness under rarely experienced, exceptionally severe conditions. The combinations analysed are:

- Pressurisation + 9g longitudinal + 3g lateral: simulates an extreme deceleration event like a hard emergency landing or sudden stop with lateral gusts, representing a rare but severe inertial load the tank must withstand.
- Pressurisation + 6g vertical downward + 3g lateral: replicates severe downward vertical acceleration combined with lateral loading, simulating turbulence or rapid descent and imposing compressive and shear stresses.
- Pressurisation + 2.5g vertical upward + 1.5g longitudinal: represents significant upward and forward acceleration during steep climbs or pull-ups under pressurised conditions, testing structural integrity during dynamic ascent.

Summary of Load Cases Analysed

The selected load cases addressed in the numerical work are summarised in Table 4:

Table 4: Summary of Load Cases Considered in the Analysis

Case	Description	Loads Applied
1	Storage pressurisation	Pressurisation only
2a	Severe manoeuvre (vertical)	Press. + 2.5 g vertical
2b	Severe manoeuvre (longitudinal)	Press. + 1.5 g longitudinal
2c	Severe manoeuvre (lateral)	Press. + 3 g lateral
3a	Extreme man. (long. + lat.)	Press. + 9 g long. + 3 g lat.
3b	Extreme man. (vert. down + lat.)	Press. + 6 g vert. down + 3 g lat.
3c	Extreme man. (vert. up + long.)	Press. + 2.5 g vert. up + 1.5 g long.

Scope and Limitations

Thermal loads have been deliberately excluded from the present preliminary analysis. This methodological choice is justified by the fact that the proposed tank design incorporates advanced MLI and cryogenic barrier systems, which significantly mitigate heat transfer and decouple thermal strains from the structural load-bearing skin. Recent studies on cryogenic tank systems [66] confirm that modern insulation permits initial structural assessments to focus primarily on mechanical load conditions. Nevertheless, it is acknowledged that fully coupled thermo-mechanical effects, such as gradients due to liquid hydrogen boil-off or cooldown transients, must be revisited in subsequent phases of design.

3.3 FEM analisis

The finite element analysis is conducted through a two-stage modelling approach to balance computational efficiency and accuracy. The first stage involves a global FEM model of the entire LH_2 storage tank, developed in Abaqus, to identify the regions experiencing the highest loads and stress concentrations under operational conditions, as shown on the left in Figure 9. Based on these results, detailed submodels with refined mesh are generated, also in Abaqus, focusing specifically on critical weld areas to accurately analyse crack initiation and propagation mechanisms, as illustrated on the right in Fig. 9. This hierarchical modelling strategy enables a precise evaluation of structural integrity and fatigue life while managing computational resources effectively.

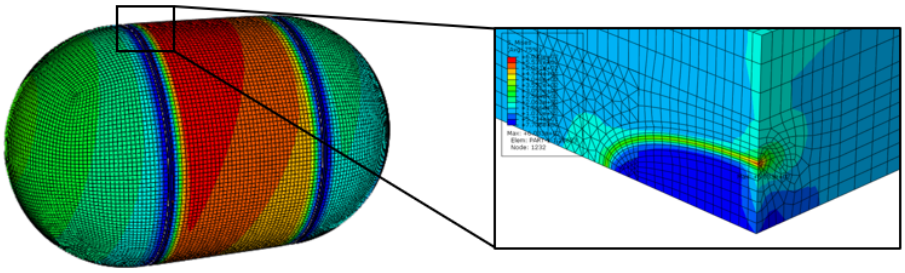


Figure 9: Global model identifies critical stress regions (left), which are further analysed via a refined submodel for local stress and crack propagation assessment (right)

3.3.1 Global FEM

The structural integrity assessment of the LH_2 storage tank is conducted using a global finite element model, ensuring the tank's capability to withstand the most critical load scenarios defined in the 2.4 Load Cases Definition.

Given that the tank walls are thin relative to their overall dimensions, the structure is modelled using shell elements rather than fully three-dimensional solid elements. This approach is standard in cryogenic tank analyses and effectively captures the mechanical behaviour of thin-walled structures while significantly reducing computational costs.

The tank walls and frames are modelled with shell elements, with the frames assigned increased thickness values to represent their higher stiffness and load-carrying capacity. Hexahedral (hex) elements are preferred for meshing due to their superior accuracy and convergence characteristics in structural FEM. A mesh convergence study was performed to determine the optimal element size, ensuring aspect ratios remain below 2 and providing reliable results without unnecessary computational expense.

Boundary conditions consider the tank as a non-integral structure attached to the fuselage via bolted connections at frames. To simplify the model, the fuselage frames are idealised as fixed supports, constraining translation and rotation. This assumption is conservative; however, it may neglect local flexibility in the fuselage structure.

Pressurisation loads are applied as uniform internal pressure on the tank surfaces. Inertial loads are modelled by defining a pressure field varying linearly with height, representing hydrostatic pressure resulting from acceleration effects during manoeuvres:

$$p = g \cdot \rho \cdot h \tag{5}$$

where:

- g is the inertial acceleration magnitude in the direction of interest,
- ρ is the density of liquid hydrogen,
- h is the distance variable measured from a reference point within the tank along the direction of the inertial acceleration (which may be vertical, longitudinal, or lateral).

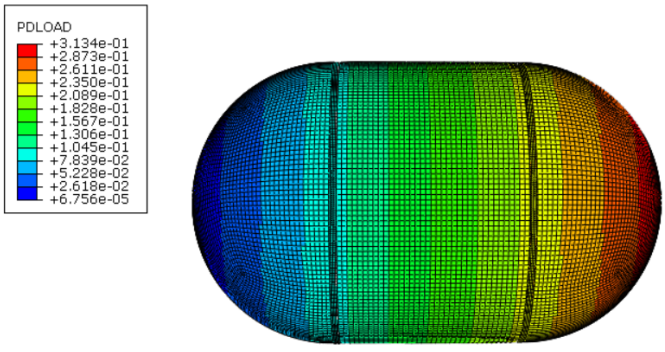
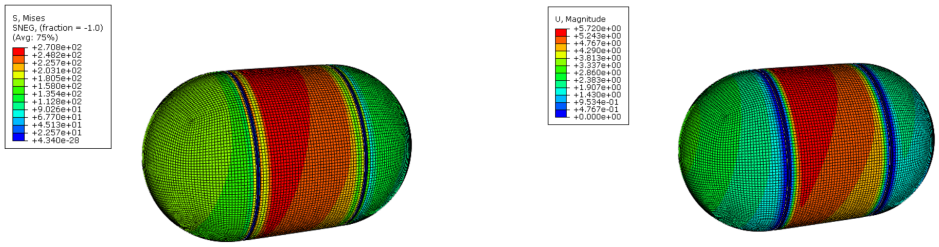


Figure 10: Schematic representation of hydrostatic pressure variation in the tank due to inertial longitudinal acceleration

The pressurisation load case results indicate a maximum Von Mises stress of 172.1 MPa, which aligns well with the preliminary design calculations detailed in 2.3.1 Minimum Thickness Calculation. This agreement provides confidence in the accuracy of the global FEM model and confirms its suitability for identifying regions of critical stress.

For the severe manoeuvre load cases, combinations of inertial accelerations result in increased maximum stresses. The worst-case scenario, involving the highest combined inertial loads, produces a maximum stress of 270.8 MPa at the weld between the frame and the cylindrical section, corresponding to a safety factor of 1.26. These values confirm that the tank maintains structural integrity across all analysed conditions. Regarding deformation, the maximum displacement observed is 5.72 mm, which is within acceptable limits given the tank's structural requirements, as it represents a small fraction of the overall tank dimensions and does not compromise structural stability.

The results of the worst-case scenario are shown in the figure below, while the remaining cases are detailed in Appendix D. For convenience, a summary of all results is presented in Table 5.



a) Max VM stress: 270.8 MPa b) Max deformation: 5.72 mm

Figure 11: Results under 3a load case

Table 5: Global FEM analysis results summary for different load cases

Load case	Maximum VM stress (MPa)	Maximum deformation (mm)	SF
1	172.1	3.58	1.98
2a	191.6	4.08	1.78
2b	195.5	4.18	1.74
2c	184.8	3.85	1.84
3a	270.8	5.72	1.26
3b	233.8	5.16	1.45
3c	204.2	4.31	1.67

In line with the literature[71], welded areas are considered most critical due to potential flaws and stress concentrations. The analysis identifies the weld between the cylindrical shell and dome as having the highest stress levels. FEM analyses will focus on crack initiation and propagation at these critical welds. Refined submodels with fracture mechanics techniques will evaluate stress intensity factors and predict crack growth, ensuring reliable fatigue life assessment. Submodelling is particularly effective for localised damage, allowing higher mesh density and precision in critical areas without greatly increasing computational cost. This approach combines global and local perspectives for a comprehensive structural assessment.

3.3.2 Crack Definition

The objective of the submodel is to study the evolution of the Mode I stress intensity factor for different crack sizes. To this end, a preliminary understanding of crack behaviour was developed, and the related parameters were benchmarked against data available in the literature to ensure a realistic representation of the phenomenon under study.

1.Material properties

Material properties play a key role in accurately predicting fracture behaviour, and these properties are not uniform in welded joints. As reported in [53,55,56,72], the elastic modulus, yield strength, and fracture toughness vary significantly across NZ, TMAZ, and HAZ, largely due to thermal cycling and microstructural gradients. In addition, fatigue crack growth parameters (Paris law constants C and m) are zone-dependent [59]. The specific width and spatial arrangement of each zone, as employed in the present study, is illustrated in Fig. 12. Table 20 summarises the mechanical properties adopted for the FEM analysis.

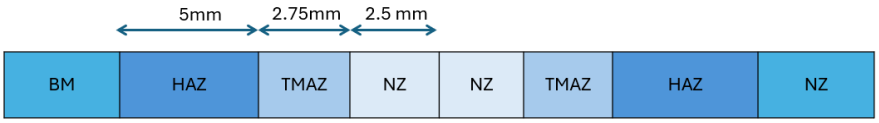


Figure 12: Zones and Spacing Distribution in FSW Weld

Table 6: Mechanical Parameters for Different Regions of the Weld

Zone	E (GPa)	Poisson (–)	J (kJ/m^2)	Max Principal Stress (MPa)	Distance from centre (mm)
NZ	70	0.33	28	295	2.5
TMAZ	70	0.33	22.5	250	5.25
HAZ	72	0.33	32	292.5	10.25
BM	72	0.33	40	477.5	—

2.Crack initiation zone

Experimental and computational studies in the literature report that cracks in friction stir welds can initiate in several microstructural zones: NZ [57,72], TMAZ [59], or HAZ [56]. While many studies suggest that TMAZ is the most common site for crack initiation due to its heterogeneous microstructure and residual stress concentration, the present study adopts a conservative assumption by placing the initial crack within NZ. This choice is justified by the higher fatigue crack growth parameter m observed for NZ, which leads to a faster crack propagation rate [59]. Modelling the crack in the most critical region ensures that the analysis represents a worst-case scenario, thereby improving the safety margin in the design evaluation. The schematic in Fig.13 illustrates the location of the crack initiation zone adopted for the FEM submodel.



Figure 13: Schematic Representation of the Crack Initiation Zone

3.Direction

The dominant service load for the welded structure is the circumferential stress, which is approximately twice the magnitude of the longitudinal stress under internal pressurisation loading. This stress state would theoretically promote the growth of longitudinal cracks. However, since the initial defect is assumed to originate from a weld region imperfection, initial consideration was given to cracks aligned along the weld line, parallel to the maximum principal stress. Nevertheless, as shown in [73,74], the actual crack propagation path is predominantly governed by the direction of the maximum principal stress, rather than by material inhomogeneity alone.

Therefore, in accordance with fracture mechanics principles, the crack was modelled perpendicular to the circumferential stress, ensuring that the model captures the most critical mode I loading condition [73]. This configuration is depicted in Fig.14, where the dominant circumferential stress (σ_c) is shown to be double the longitudinal stress (σ_l), and the assumed crack propagation direction is aligned accordingly.

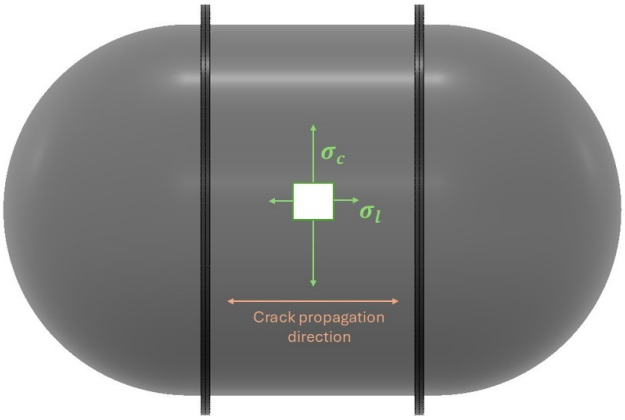


Figure 14: Schematic Representation of Circumferential (σ_c) and Longitudinal (σ_l) Stresses in the Tank

4.Crack geometry

Across the reviewed literature, the semi-elliptical surface crack is identified as the most representative geometry for cracks in welded plates subjected to bending or pressure loading [57,58] [58,75]. Following the observations of previous studies, the aspect ratio (a/b) between the crack depth (a) and the half-surface length (b) typically evolves from approximately 0.3 during the initiation phase to around 0.5 during propagation [76,77].

In this work, the analysis begins with four initial crack sizes. To refine the correlation between K_I and crack length, an additional four intermediate crack geometries were studied. This progressive refinement ensures that the resulting curve accurately captures the non-linear trends in fracture mechanics response. Fig.15 presents a schematic overview of the eight different crack geometries analysed, illustrating their locations within the weld zones (BM, HAZ, TMAZ, NZ) and how the crack size progresses during the study.

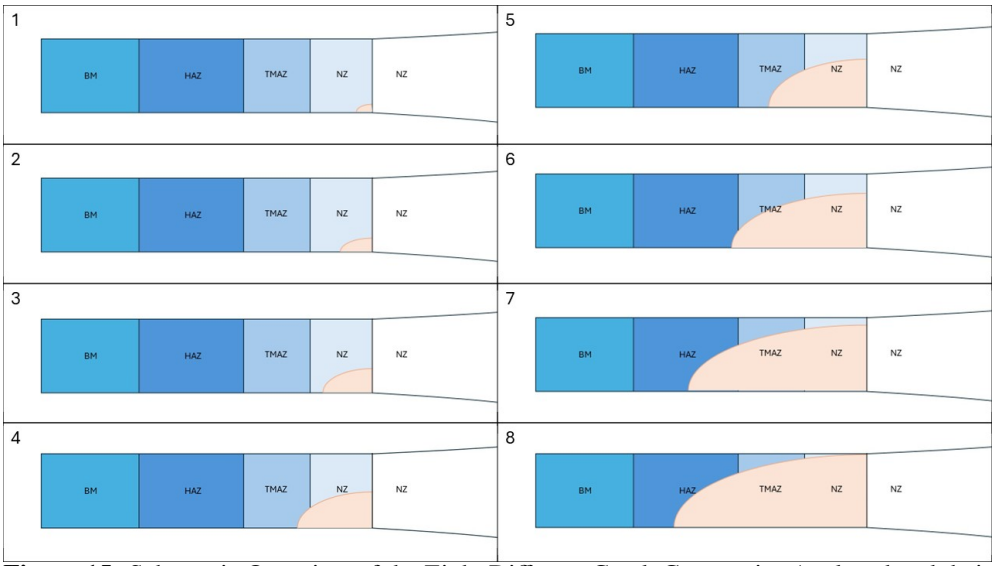


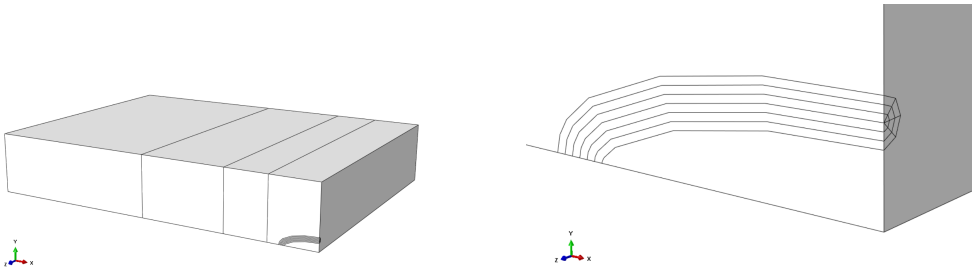
Figure 15: Schematic Overview of the Eight Different Crack Geometries Analysed and their Locations within the Weld Zones

3.3.3 Detailed FEM

With the analytical crack definitions and material properties established, the next step involves constructing the detailed FEM model, including mesh refinement and boundary condition application, to accurately compute stress intensity factors and assess crack growth behaviour.

First, the welded joint was divided into distinct material zones, with each zone assigned specific mechanical properties to properly capture the material heterogeneity. This partitioning ensures that the model reflects the actual variation in mechanical response across the weld.

The crack front was discretised into segments to enable focused mesh refinement. By dividing the crack into multiple parts, the mesh density could be selectively increased near the crack tip, which is essential for accurately resolving the stress singularities characteristic of fracture mechanics problems. This process is illustrated in Fig. 16.



a) Weld Zones b) Crack Front

Figure 16: 3D Submodel Partitioning:

The crack itself was modelled with a semi-elliptical geometry. The Mode I stress intensity factor, K_I, was calculated using the contour integral method, commonly known as the J-integral, applied along several contours closely surrounding the crack tip. This approach provides a path-independent and reliable evaluation of K_I, which is critical for fracture analysis.

A meticulous meshing strategy was employed, involving progressively finer mesh elements concentrated around the crack tip to achieve numerical convergence while managing computational costs. Near the crack front, special singular or focused elements were likely used to capture stress gradients with high accuracy.

Service loads consistent with the global FEM results were applied. At the interface between the submodel and the global model, boundary conditions were imposed to constrain displacements as necessary, ensuring continuity between the refined region and the overall structure. Along the crack surface, movement perpendicular to the crack plane was restricted to realistically simulate crack face behaviour under loading.

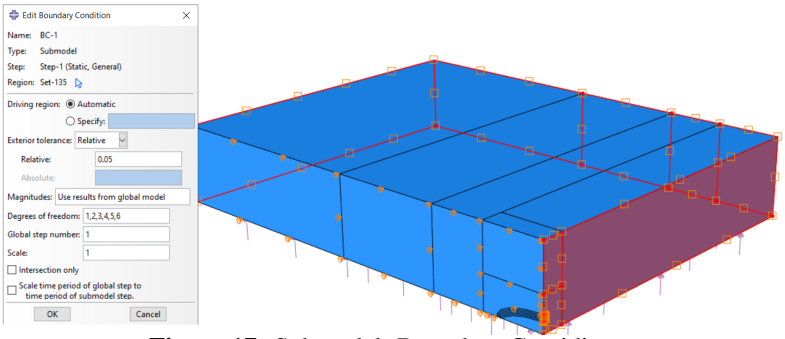


Figure 17: Submodel: Boundary Contidions

Finally, multiple extraction points were placed along the crack front to record the spatial distribution of K_I. For each crack size, all computed K_I values were collected and documented (with full datasets available in Appendix E). The maximum K_I value along the crack front was selected as the representative parameter for fracture assessment, typically occurring near the intersection of the crack with the free surface.

Analysis Procedure and Output Processing

The described procedure was applied to all eight modelled crack sizes, maintaining consistent boundary conditions, mesh refinement, and material property assignments to ensure accurate and comparable results. For each configuration, the maximum Mode I stress intensity factor along the crack front was extracted from the numerical output. These maximum K_I values were then correlated with their respective crack lengths to construct the K_I versus a (crack length) relationship. This relationship serves as the fundamental input for fatigue crack growth assessment and is illustrated in Fig. 18.

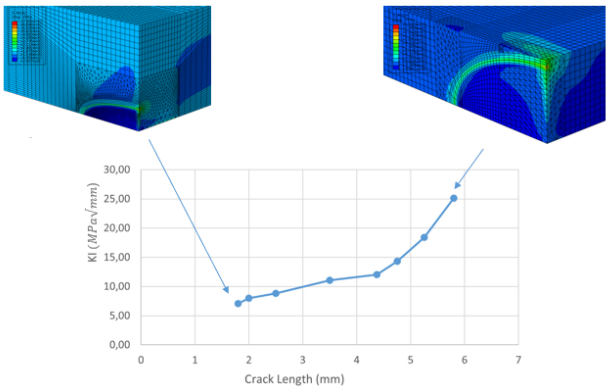


Figure 18: Relation between Mode I stress intensity factor, K_I, and crack length, a (mm).

Within this context, failure is defined as occurring either when the stress intensity factor K_I reaches the material's fracture toughness K_{IC}, or when the crack length exceeds the material thickness. The latter case is critical because through-thickness crack penetration can cause leakage.

For the Heat Affected Zone, the calculated stress intensity factor at the point of full thickness penetration is

$$K_I = 25.13 \text{ MPa} \sqrt{\text{mm}},$$

while the fracture toughness of the material is

$$K_{IC} = 27.5 \text{ MPa} \sqrt{\text{mm}}.$$

Since $K_I < K_{IC}$, failure in this case is governed by crack penetration through the thickness rather than by exceeding the material's fracture toughness.

3.4 Classical Fatigue Life Calculation and Damage Tolerance

The fatigue life of metallic structures is generally divided into two principal phases: crack initiation and crack propagation. The initiation phase involves the accumulation of microstructural damage under cyclic loading until a crack becomes detectable, whereas the propagation phase describes the growth of this crack until failure[39]. For aluminium alloys and welded joints, initiation is often the dominant portion, representing up to 70–90% of total fatigue life[38].

In this study, a conservative 50% of the total fatigue life (N_f) is allocated to crack initiation, reflecting both methodological assumptions and the limited relevant experimental data under cryogenic service conditions. A damage tolerance approach assumes an initial microscopic flaw of 0.02 mm within the critical weld region, consistent with engineering standards and typical nondestructive inspection capabilities[78].

The adopted fatigue life assessment methodology follows the dual-phase workflow presented in Fig.19, combining classical fatigue life estimation to crack initiation using S-N data, and fracture mechanics-based crack propagation analysis utilising Paris law parameters specific to friction stir welded aluminium alloys at cryogenic temperatures. This complementary approach enables a thorough evaluation of structural durability.

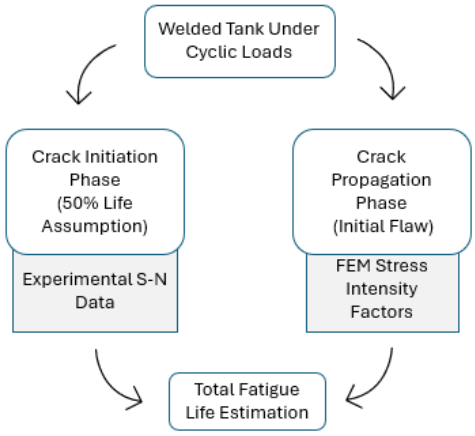


Figure 19: Workflow Diagram of Dual-phase Fatigue Life Assessment Methodology

3.4.1 Classical Fatigue Life Calculation

Crack initiation modelling for the AA2219-T87 aluminium alloy was undertaken using S-N data sourced from the literature[79] (see Fig. 20), which correlates the applied service stress amplitude to the corresponding fatigue life in cycles,N_f.

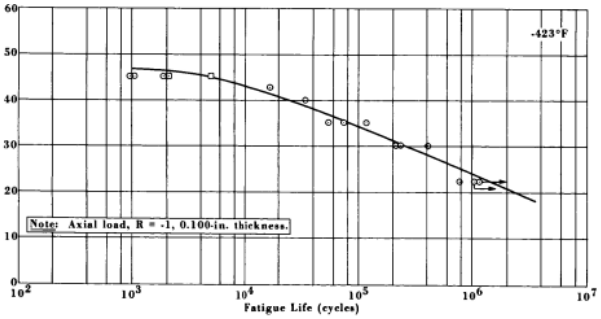


Figure 20: S-N data for 2219-T87 welded under cryogenic temperature conditions Stress Range (ksi) vs Number of Cycles (N)[79].

The available S-N dataset for cryogenic testing was obtained from experiments conducted on TIG welded joints under a load ratio of $R = -1$, representing fully reversed tension–compression loading. Although the present study focuses on friction stir welded (FSW) joints, the use of TIG-based S-N data introduces a degree of conservatism. FSW joints have been demonstrated to outperform TIG welds in fatigue performance owing to their finer microstructure and absence of solidification defects[31]. Therefore, TIG fatigue data provide a safe lower bound for fatigue life estimation in the absence of direct cryogenic test data for FSW joints.

Furthermore, the application of S-N data obtained at a load ratio of $R = -1$ to predict fatigue life under tension–tension loading conditions with R values ranging from 0 to 0.9 is an accepted engineering approximation. For the same maximum stress magnitude, fully reversed loading results in a larger cyclic stress range compared to tension–tension loading, effectively doubling the stress amplitude, thus leading to shorter fatigue lives. Since a positive mean tensile stress ($R > 0$) generally reduces crack opening and delays crack initiation, basing life predictions on $R = -1$ data provides a conservative estimate[38]. This conservative approach considering both the weld type and loading ratio ensures the inclusion of safety margins to account for potential uncertainties.

The S-N data were digitised using WebPlotDigitizer (version 5.2) and subsequently plotted on logarithmic scales to linearise the power-law relationship between stress amplitude and fatigue life. A linear regression analysis was performed on the transformed dataset, fitting a straight line of the form:

$$\log(N) = -m \log(S) + \log(C^*), \tag{6}$$

where N is the number of cycles to crack initiation, S is the applied stress amplitude, and $C^* = C^m$ for convenience in the fitting process. The regression yields the slope and intercept of the best-fit line, from which the fatigue strength exponent m is obtained as the negative of the slope, and the fatigue strength coefficient C is calculated by:

$$C = 10^{\frac{\text{intercept}}{m}}. \tag{7}$$

These parameters characterise the material's fatigue behaviour under cyclic loading. The resulting Basquin equation then allows calculation of the fatigue life N for any applied stress amplitude S as:

$$N = \left(\frac{C}{S}\right)^m. \tag{8}$$

Table 7: Load cases with corresponding stress levels and number of cycles.

Load case	**Stress [MPa]**	**Number of cycles**
Pressurisation	172	755,424
Pressurisation over pressure	174	683,353
Severe manoeuvre	195	254,365
Extreme manoeuvre	270	15,125

To assess cumulative fatigue damage under variable amplitude loading, Miner's linear damage rule was applied by considering the characteristic number of in-service cycles n_i experienced at each stress level i. The damage fraction D is calculated as:

$$D = \sum_i \frac{n_i}{N_i} = \frac{n_1}{N_1} + \frac{n_2}{N_2} + \cdots + \frac{n_k}{N_k}, \tag{9}$$

where N_i is the number of cycles to crack initiation at stress level i obtained from the Basquin equation.

Miner's rule assumes linear damage accumulation and does not account for load sequence effects, interaction between different stress levels, or potential material memory effects. Despite these limitations, it remains widely accepted in engineering practice due to its simplicity and generally conservative nature, especially when combined with adequate safety factors.

Using the specific load spectrum and cycle counts detailed in Table 19, the damage fraction was calculated as D=0.64, indicating that approximately 64% of the critical fatigue damage has already accumulated. Considering a total of 1,708,269 applied load cycles in the analysed spectrum, the estimated total fatigue life is obtained by dividing this number by the damage fraction D, yielding:

$$N_{\text{total}} = \frac{N_{\text{spectra}}}{D} = \frac{1,708,269}{0,642} \approx 2,658,725 \text{ cycles}. \tag{10}$$

Thus, the structure is expected to endure approximately 2.66 million cycles before reaching the critical fatigue damage threshold.

While the classical fatigue life calculation and Miner's rule provide a useful estimate of accumulated damage and remaining life before crack initiation, they inherently assume that the structure remains free of detectable cracks up to that point. Given the critical nature of hydrogen storage tanks, where small defects may already exist or initiate earlier, it is essential to complement this analysis with a fracture mechanics-based assessment of crack propagation and its impact on structural integrity.

3.4.2 Damage Tolerance

Unlike classical fatigue life calculations that focus on crack initiation, the damage tolerance approach directly addresses the growth of existing cracks under cyclic loading, providing essential insights into residual life and structural safety. This section outlines the methodology and key inputs required to model crack propagation.

Crack propagation analysis requires the following critical inputs:

1. The variation of the Mode I stress intensity factor K_I with crack size a (the K_I–a relationship), previously obtained from a refined finite element submodel.
2. The fatigue crack growth rate parameters of the material, namely C and m, taken from the literature[59] .

These inputs are then used to implement the Paris–Erdogan law:

$$\frac{da}{dN} = C \cdot (\Delta K)^m, \tag{11}$$

where $\frac{da}{dN}$ is the crack growth rate per cycle and ΔK is the stress intensity factor range.

Experimental studies have shown significant variability in fatigue crack growth rates across friction stir welded aluminum joints due to spatial differences in grain structure, hardness, and residual stresses[72,59]. Accordingly, distinct Paris law parameters are applied to each weld zone: NZ, TMAZ, and HAZ.

Crack growth data for cryogenic FSW aluminum joints were digitised from Fig. 7 using WebPlotDigitizer (version 5.2). For each weld zone, the data were linearised on logarithmic scales, and the Paris parameters m and C were obtained through regression analysis in MATLAB (see Table 8).

To account for the cryogenic condition (−253°C), adjustment factors from previous studies were applied proportionally[64]. The modified Paris parameters are hereafter referred to as m' to distinguish them from the baseline values.

Table 8: Paris law parameters for FSW aluminium joints under cryogenic conditions

Zone	m	**Adjusted** m'
NZ	3.30	3.84
TMAZ	3.08	3.58
HAZ	3.08	3.58

Zone-by-Zone Propagation Simulation

Utilising the zone-specific Paris law parameters alongside the FEM-derived K_I–a curve, crack growth was simulated incrementally across the weld, sequentially progressing from the NZ through the TMAZ to the HAZ. Due to the absence of direct experimental crack growth data in the HAZ, and considering its typically higher crack propagation rates, the Paris parameters for the TMAZ were conservatively applied to the HAZ.

The total number of fatigue cycles N required for crack growth from an initial length a_i to a final length a_f in each weld zone was calculated via numerical integration of Paris' law. Crack growth in the nugget zone was considered from the minimum detectable crack length up to the transition into the TMAZ. In turn, the TMAZ was modelled from its onset until the beginning of the HAZ, and finally, the HAZ was analysed from its start until the crack reached the full plate thickness.

$$N = \int_{a_i}^{a_f} \frac{1}{C\,[\Delta K(a)]^m}\,da, \tag{12}$$

where N denotes the total number of cycles required for crack growth between the initial length a_i (onset of fatigue crack growth) and the final length a_f (critical crack length at failure). The parameters C and m are the Paris coefficients corresponding to each weld zone, while $\Delta K(a)$ represents the stress intensity factor range as a function of crack length.

This integration was implemented in MATLAB, employing the zone-specific Paris parameters, FEM-derived K_I data, and prescribed crack length increments.

The total crack propagation life N_p was obtained by summing the calculated cycles for crack growth through each weld zone:

$$N_p = N_{\mathrm{NZ}} + N_{\mathrm{TMAZ}} + N_{\mathrm{HAZ}}. \tag{13}$$

The results of this crack propagation simulation are presented and discussed in 3.3 Damage Tolerance Analysis section, providing critical insight into the damage tolerance behaviour.

4.0 Results and discusion

4.1 Validation of Finite Element Model

The finite element model developed for the LH_2 tank was validated against hand calculations performed for the pressurisation load case. These hand calculations, based on classical pressure vessel theory, provided analytical estimates of the maximum hoop and longitudinal stresses.

The comparison focused on the points of maximum tension identified in the FEM results under the pressurisation load. Good agreement was observed, with a deviation of approximately 11% (see Table 9). This difference is attributed to the FEM's ability to account for local stress concentrations, which are not captured by the simplified analytical approach.

Table 9: Comparison of stress results from hand calculation and FEM analysis

Analysis type	**Stress (MPa)**
Hand calculation	192.9
FEM analysis	172.1
Deviation	11%

Furthermore, the finite element model not only confirmed the analytical stress levels but also provided a detailed picture of the stress distribution across the tank structure, which is essential for predicting potential crack initiation areas. Unlike the uniform stress fields assumed in classical pressure vessel theory , the FEM allowed the identification of local tensile and compressive regions, thereby highlighting critical zones where stress concentrations may favor damage onset[71].

4.2 Classical Fatigue Life Calculation

The classical fatigue life estimation, based on the applied load spectrum and Miner's cumulative damage rule, yielded a total fatigue life of approximately 2.66 million cycles.

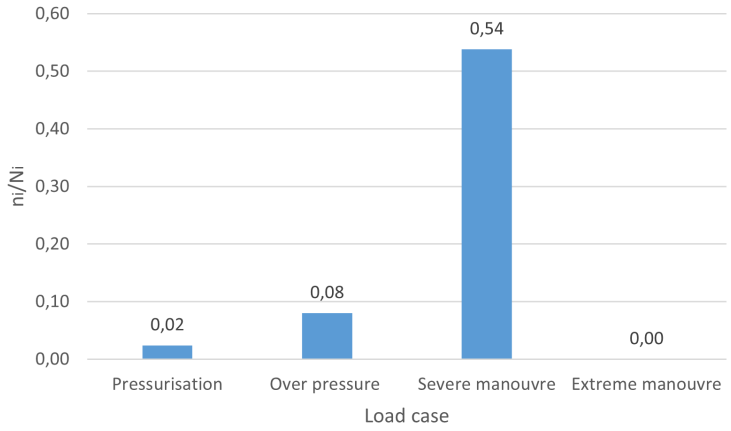


Figure 21: Damage fraction ($\frac{n_i}{N_I}$) accumulated under each load case.

Severe manoeuvres, although less frequent than venting pressurization or pressurization cycles, induce higher stress amplitudes that cause greater cumulative damage. Load cases associated with these highest stress amplitudes, such as severe manoeuvres, exert the greatest influence on Miner's damage accumulation, despite their lower frequency compared to pressures generated during venting. This effect is illustrated in Fig. 21, which displays the contribution of each load case to the overall damage fraction.

Overall, the classical fatigue approach suggests that crack initiation under the specified operational spectrum would require a large number of cycles, confirming the inherent durability of the AA2219-T87 alloy under cryogenic conditions and the conservative assumptions employed in this analysis. If crack initiation is assumed to constitute 50% of the total fatigue life, the initiation phase would last approximately 1.33 million cycles. The subsequent crack propagation phase is analysed using a damage tolerance approach in the following section.

4.3 Damage Tolerance Analysis

In striking contrast, the damage tolerance approach predicts a fatigue crack propagation life of approximately 12,000 cycles, starting from an initial microscopic flaw of 0.02 mm up to critical failure, assumed when the crack reached the tank thickness, which occurs before the stress intensity factor reaches K_{IC}.

A detailed examination of crack propagation lifetimes calculated using the baseline exponent m and its adjusted counterpart m' reveals that incorporating cryogenic effects decreases life estimates by approximately 57%, underlining the crucial need to consider environmental influences in damage tolerance assessments as shown in Fig. 22.

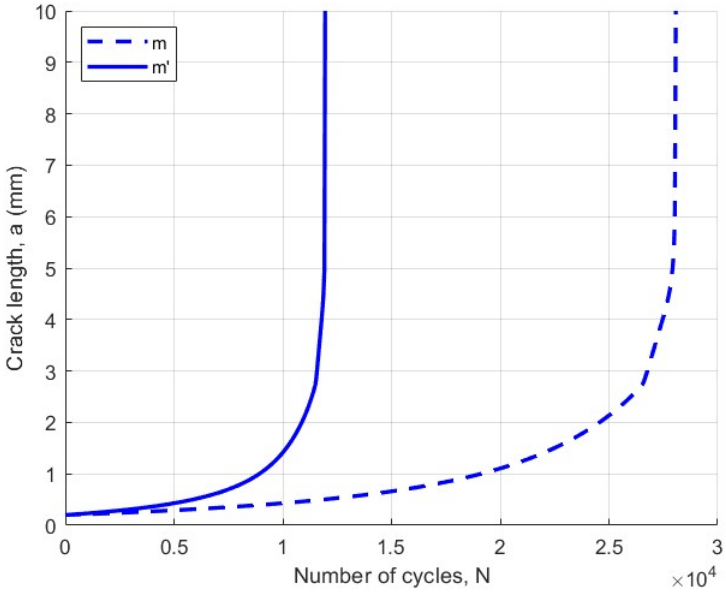


Figure 22: Crack growth (a vs N) - Comparison between m and m'

The crack propagates more rapidly in the TMAZ and HAZ despite having a lower Paris law exponent m compared to the NZ. This accelerated propagation occurs because the stress intensity factor K_I reaches higher values due to the larger crack size in these zones, which compensates for the reduced material sensitivity to crack growth. This behaviour is clearly illustrated in Fig. 23.

Furthermore, an important observation emerges when analysing the blue dotted line, which represents the crack propagation behaviour considering only the NZ parameters throughout the entire specimen. This idealized scenario predicts a lower total number of cycles to failure compared to the realistic case that incorporates the specific Paris law parameters for each zone (TMAZ and HAZ). This comparison underscores the critical importance of implementing zone-specific material parameters that account for microstructural heterogeneity in welded joints. Neglecting these variations would lead to non-conservative predictions that underestimate crack propagation rates and overestimate the fatigue life of the component.

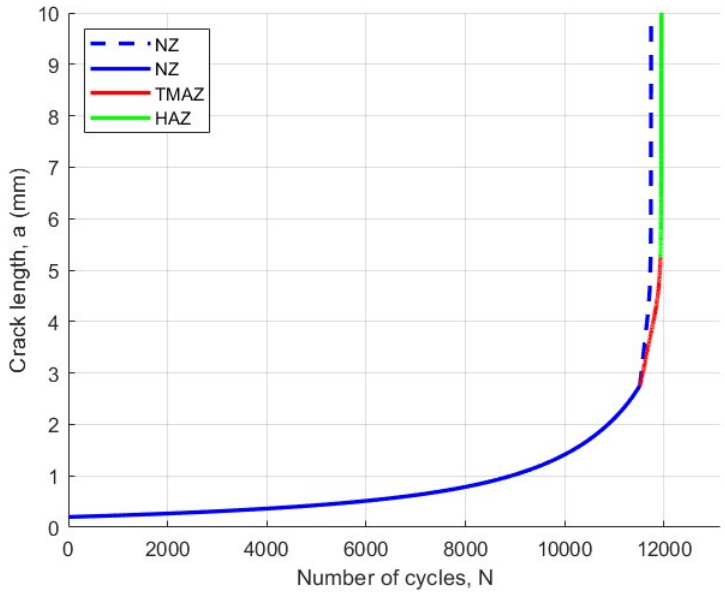


Figure 23: Crack growth (a vs N) - Comparison between FSW Different Zones (NZ, TMAZ and HAZ) or Constant NZ

These results complement the classical fatigue life estimation presented earlier, which focused on crack initiation. Together, they provide a comprehensive understanding of the total fatigue life of the LH_2 tank weld joints, bridging the gap between fatigue initiation and growth phases under realistic cryogenic service environments.

4.4 Discussion on Fatigue Life Perspectives

The results clearly underscore the dual and complementary nature of fatigue life assessment methods. From an academic perspective, these findings align with extensive literature reporting that AA2219-T87 aluminium alloy exhibits a notably low fatigue threshold ΔK_{th} [41]. This low threshold explains why the crack initiation phase can encompass a substantial portion of the total fatigue life, often spanning millions of loading cycles even under demanding service conditions.

Conversely, once a crack initiates, crack propagation proceeds rapidly, particularly through the heterogeneous microstructural zones of the weld. This accelerated growth is markedly exacerbated by the combined effects of cryogenic temperatures and exposure to hydrogen environments, both of which are documented to degrade fatigue crack growth resistance significantly [64]. Such environmental factors reduce Paris law parameters and shorten propagation life, as evidenced in the adjusted parameters and reduced cycle counts observed in this study.

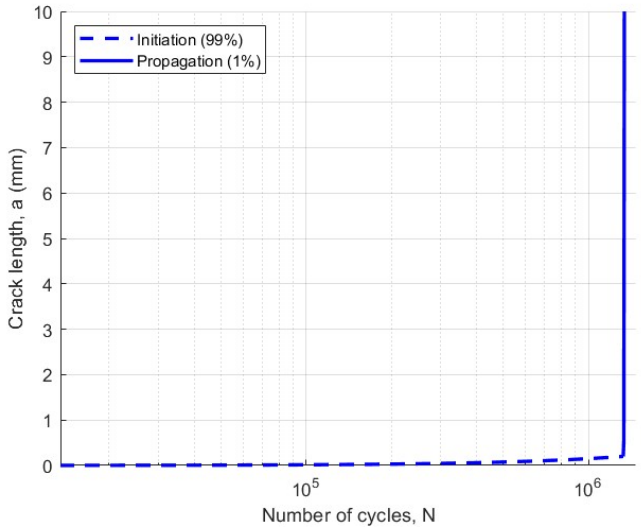


Figure 24: Crack growth (a vs N) - Initiation (99%) and Propagation(1%)

From a practical engineering standpoint, given the criticality of the LH_2 storage tank, fracture control and damage tolerance principles should guide the fatigue life assessment and maintenance strategies. While classical fatigue life models remain valuable for understanding initiation behaviour, the brief crack propagation life mandates that inspection and monitoring protocols prioritise early detection and management of cracks, as even minor defects can lead not only to structural failure but also to leakage of highly flammable LH_2, posing serious safety and operational risks.

Incorporating damage tolerance frameworks as the basis for inspection intervals and structural integrity evaluations ensures that the accelerated risk associated with crack growth under cryogenic hydrogen service is effectively mitigated. This approach aligns with best practice in safety-critical components subjected to harsh environments, providing a robust basis for risk-informed maintenance and operational planning.

5.0 Conclusions and Future Work

5.1 Conclusions

The present work has developed a comprehensive analysis of fatigue behaviour in liquid hydrogen storage tanks constructed from AA2219-T87 aluminium alloy with FSW joints, addressing both the classical crack initiation phase and crack propagation through a damage tolerance approach. The main conclusions can be summarised as follows:

Conservatism and Potential Overestimation: Due to the limited availability of experimental data under cryogenic conditions with hydrogen exposure, current fatigue life assessments rely on conservative assumptions and elevated safety factors. This approach may lead to an overestimation of the component's fatigue performance, particularly during the crack initiation phase, underscoring the need for targeted testing and refined methodologies to improve prediction accuracy.

Marked Difference Between Initiation and Propagation: Although the rapid crack propagation relative to the lengthy initiation phase aligns with fracture mechanics principles and existing literature, the relatively short propagation life is further accentuated by the thin wall thickness of the tank. Consequently, cracks tend to penetrate the full thickness before reaching the critical stress intensity factor K_I, posing a significant risk to structural integrity. The implementation of surface coatings or barriers to mitigate leakage risk warrants further consideration.

Effects of Hydrogen and Cryogenic Environment on Material Behaviour: Exposure to hydrogen in combination with cryogenic temperatures significantly alters material properties and fatigue behaviour, accelerating crack growth and potentially changing failure mechanisms. These service conditions cannot be reliably inferred from conventional data, highlighting the importance of dedicated studies that directly address the effects of hydrogen and extreme low temperatures on structural materials.

Current Limitations for Commercial Implementation: While hydrogen represents a promising sustainable aviation fuel, the spatial demands imposed by the storage tanks and the detrimental effects of hydrogen on material durability introduce substantial structural and design challenges. Addressing these concerns requires a holistic approach that integrates structural engineering with aerodynamic, economic, and environmental considerations to ensure true feasibility and sustainability.

Importance of Rigorous, Multidisciplinary Analysis: Throughout the literature review and study development, it became apparent that diverse sources can offer conflicting or disparate results and methodologies. This situation underscores the critical importance of performing a thorough and critical review of multiple studies, ensuring that conclusions are grounded in the best available evidence and maintain internal consistency.

5.2 Future Work

Considering the present limitations and the requirement for accurate and reliable assessments to safeguard safety and operational efficiency, the following research directions are suggested:

1. **Implementation of Targeted Experimental Testing:** Conduct fatigue and crack propagation experiments on FSW aluminium specimens under cryogenic temperatures and direct hydrogen exposure to obtain empirical data for validation and refinement of life prediction models.
2. **Integration of Thermal and Combined Loading:** Extend the numerical modelling framework to incorporate transient thermal effects and combined mechanical-thermal loading representative of real service conditions in LH_2 tanks.
3. **Buckling Analysis:** Investigate the susceptibility of the tank to buckling under relevant service loads, including cryogenic conditions and hydrogen pressure. This study should encompass numerical stability analyses to identify critical buckling modes and load thresholds. The results will provide insight into structural integrity and inform design considerations to prevent premature failure due to buckling phenomena.
4. **ASME-Based Welding Assessment:** Evaluate the welds according to ASME Boiler and Pressure Vessel Code standards, particularly Section IX for welding qualifications and Section VIII for pressure vessel requirements. This assessment will compare structural performance and fatigue resistance obtained from experiments and simulations with code-allowed values. The aim is to verify compliance and identify potential gaps or conservatisms in using ASME criteria for FSW aluminium joints in cryogenic hydrogen tank applications.
5. **Development of Advanced Monitoring Systems:** Propose and develop advanced non-destructive evaluation techniques and continuous structural health monitoring technologies, including the use of fibre optic sensors, for early crack detection to improve safety and optimise maintenance practices.

6.0 Acknowledgements

I would like to express my deepest gratitude to my supervisor, Ioannis Giannopoulos, for his invaluable guidance, support, and encouragement throughout the development of this thesis. His ability to skilfully steer the project while allowing the objectives and direction to evolve organically based on emerging findings has been greatly appreciated. His expertise and constructive feedback have been instrumental in shaping this work.

I am also thankful to my classmates who have provided support and assistance during this individual research project, especially Sakshi, who, despite not working directly with me on this project, has been an incredible companion and source of encouragement throughout this journey. I am equally grateful to my friends at Cranfield for welcoming me like family and offering their warmth and kindness over these months.

I would also like to extend my gratitude to my partner, whose understanding and support during the most demanding stages of this thesis have been deeply valuable.

Finally, I would like to thank my family for their unwavering patience and encouragement throughout this challenging journey, and for giving me the opportunity to pursue and achieve my goals.

References

1. P. Friedlingstein et al. Global carbon budget 2023. *Earth System Science Data*, 15:5301–5369, 2023.
2. Khurram Shahzad and Izzat Iqbal Cheema. Low-carbon technologies in automotive industry and decarbonizing transport. *Journal of Power Sources*, 591:233888, 2024.
3. European Union Aviation Safety Agency. European aviation environmental report 2025: Executive summary and recommendations. Technical report, European Union Aviation Safety Agency (EASA), 2025. Accessed August 2025.
4. Eytan J. Adler and Joaquim R. R. A. Martins. Hydrogen-powered aircraft: Fundamental concepts, key technologies, and environmental impacts. *Progress in Aerospace Sciences*, 141:100922, 2023. Special Issue on Green Aviation.
5. Talal Yusaf, Abu Shadate Faisal Mahamude, Kumaran Kadirgama, Devarajan Ramasamy, Kaniz Farhana, Hayder A. Dhahad, and Abd Rahim Abu Talib. Sustainable hydrogen energy in aviation – a narrative review. *International Journal of Hydrogen Energy*, 52:1026–1045, 2024.
6. F. Santos, M. Pérez, and J. Smith. Hydrogen propulsion systems for aircraft: A review on recent advancements. *International Journal of Hydrogen Energy*, 49:12345–12367, 2024.
7. GreenAir News. Airbus delays its zeroe hydrogen aircraft with 5–10 year timeline extension, 2025. Report confirms delay of hydrogen commercial aircraft introduction due to technological and ecosystem challenges.
8. M. Soleymani, V. Mostafavi, M. Hébert, S. Kelouwani, and L. Boulon. Hydrogen propulsion systems for aircraft: A review on recent advances and ongoing challenges. *International Journal of Hydrogen Energy*, 91:137–171, 2024.
9. G. D. Brewer. *Hydrogen Aircraft Technology*. Routledge, 1 edition, 1991.
10. Jon Huete and Pericles Pilidis. Parametric study on tank integration for hydrogen civil aviation propulsion. *International Journal of Hydrogen Energy*, 46, 2021.
11. Rodolfo Taccani, Stefano Malabotti, Chiara Dall'Armi, and Diego Micheli. High energy density storage of gaseous marine fuels: An innovative concept and its application to a hydrogen powered ferry. *International Shipbuilding Progress*, 67(2):113–136, 2020.
12. B. Okpeke, A. Kamble, N. Dahiya, G. Spangardt, and S. Niemi. Assessment of boil-off losses and their cost implication during liquid hydrogen bunkering. *Energies*, 17(16):4092, 2024.
13. W. Notardonato, W. Johnson, Adam Swanger, and Thomas Tomsik. Ground operations demonstration unit for liquid hydrogen: Initial test results. *IOP Conference Series: Materials Science and Engineering*, 101(1):012081, 2015.
14. G. Onorato, P. Proesmans, and M. F. M. Hoogreef. Assessment of hydrogen transport aircraft: Effects of fuel tank integration. *CEAS Aeronautical Journal*, 13(4):813–845, 2022.
15. Mehdi Soleymani, Vahid Mostafavi, Marie Hebert, Sousso Kelouwani, and Loïc Boulon. Hydrogen propulsion systems for aircraft: A review on recent advances and ongoing challenges. *International Journal of Hydrogen Energy*, 91:137–171, 2024.

16. G. D. Brewer and R. E. Morris. Study of lh2 fueled subsonic passenger transport aircraft. Contractor report nasa/cr–144935, NASA, 1976.

17. Jai Ahuja, Christian Perron, Reina D. Bermudez Rivera, Jimmy C. Tai, and Dimitri N. Mavris. Performance comparison of the blended wing body and tube-and-wing configurations. Technical report, Aerospace Systems Design Laboratory, Daniel Guggenheim School of Aerospace Engineering, Georgia Institute of Technology, 2025. Available at `https://www.icas.org/icas_archive/icas2024/data/papers/icas2024_1296_paper.pdf`.

18. Eytan J. Adler and Joaquim R. R. A. Martins. Blended wing body configuration for hydrogen-powered aviation. *Journal of Aircraft*, 61(3):1–15, 2024. Department of Aerospace Engineering, University of Michigan.

19. W. E. Witzell. Crack growth behavior of 2219-t87 aluminum alloy from 20 k (-423 °f) to 422 k (300 °f). Contractor Report CASD-NAS73-011, NASA-CR-134047, National Aeronautics and Space Administration, Lyndon B. Johnson Space Center, San Diego, California, 1973. Prepared by General Dynamics Convair Aerospace Division.

20. De-Yi Qiu et al. Research progress of cryogenic materials for storage and transportation containers of liquid hydrogen. *Metals*, 11:1101, 2021.

21. de M. Simanullang et al. Liquid hydrogen storage and insulation materials for future energy and transportation sectors. *International Journal of Hydrogen Energy*, 2025.

22. Robin Olsson, Christopher Cameron, Florence Moreau, Erik Marklund, Matthias Merzkirch, and Jocke Pettersson. Design, manufacture, and cryogenic testing of a liner-less composite tank for liquid hydrogen. *Applied Composite Materials*, 31:1–24, 2024.

23. Bicai Deng, Shaoqi Yang, Xiujuan Xie, Yunlong Wang, Xing Bian, Linghui Gong, and Qing Li. Study of the thermal performance of multilayer insulation used in cryogenic transfer lines. *Cryogenics*, 100:114–122, 2019.

24. Liang Chen, Hongyu Lv, Yuheng Shang, Ze Zhang, Shuangtao Chen, and Yu Hou. Strategies for improving the thermal insulation performance of liquid hydrogen tanks: A review of multilayer insulation structure. *International Journal of Hydrogen Energy*, 94:1419–1434, 2024.

25. Liang Yin, Haonan Yang, and Yonglin Ju. Review on the key technologies and future development of insulation structure for liquid hydrogen storage tanks. *International Journal of Hydrogen Energy*, 57:1302–1315, 2024.

26. James E. Fesmire, B. E. Coffman, B. J. Menghelli, and K. W. Heckle. Spray-on foam insulations for launch vehicle cryogenic tanks. Technical Report KSC-2011-140, NASA Kennedy Space Center and ASRC Aerospace, Kennedy Space Center, FL, USA, 2011.

27. Binhan Sun et al. Microstructure design strategies to mitigate hydrogen embrittlement in metallic materials. *Fatigue & Fracture of Engineering Materials & Structures*, 46(9):2210–2226, 2023.

28. Qian Cheng, Ruiqiang Zhang, Zhusheng Shi, and Jianguo Lin. Review of common hydrogen storage tanks and current manufacturing methods for aluminium alloy tank liners. *International Journal of Lightweight Materials and Manufacture*, 7(2):269–284, 2024.

29. Colin Bell, Jonathan Corney, Nicola Zuelli, and David Savings. A state of the art review

of hydroforming technology. *International Journal of Material Forming*, 13(5):789–828, 2020.

30. Tian Gan, Jun Ni, Zhongqi Yu, Yixi Zhao, and Shuhui Li. Study on warm formability of aluminum alloy 2219 in hemispherical part conventional spinning. *Procedia Manufacturing*, 50:45–50, 2020. 18th International Conference on Metal Forming 2020.
31. A. Squillace, A. De Fenzo, G. Giorleo, and F. Bellucci. A comparison between fsw and tig welding techniques: modifications of microstructure and pitting corrosion resistance in aa 2024-t3 butt joints. *Journal of Materials Processing Technology*, 152(1):97–105, 2004.
32. Noor Khan, Annayath Maqbool, Tariq Ahmad, Arshad Siddiquee, and Zahid Khan. Fracture behaviour of friction stir welded dissimilar aluminium alloys. *Materials Today: Proceedings*, 46:–, 2021.
33. D. Verstraete. Propulsion and power research for high-speed aircraft. *Progress in Aerospace Sciences*, 45(8):409–422, 2009. LH2 tanks operated at around 1.3–1.5 bar for vapor pressure control.
34. NASA. Reference gauging system for a small-scale liquid hydrogen tank. Technical Report TP-2003-210785, NASA, 2003. Experimental LH2 tanks maintained at 1.1–1.3 bar during tests.
35. Arturo Gomez and Howard Smith. Liquid hydrogen fuel tanks for commercial aviation: Structural sizing and stress analysis. *Aerospace Science and Technology*, 95:105438, 2019.
36. Sara Perelli and Giovanni Genna. Hazards identification and risk management of hydrogen production and storage installations. *Chemical Engineering Transactions*, 96:193–198, 2022.
37. Sam Stewart. Liquid hydrogen storage. In *Liquid Hydrogen: Properties, Production and Applications*, pages 264–298. Pergamon, 2013.
38. R. I. Stephens. *Metal Fatigue in Engineering*. Wiley, New York, 2nd edition, 2001. Electronic book.
39. S. Suresh. *Fatigue of Materials*. Cambridge University Press, Cambridge, 1998.
40. C. R. Denaburg. Low temperature mechanical properties of aluminum alloy 2219-t87, 0.040-inch thick sheet through 5.000-inch thick plate; low temperature mechanical properties of aluminum alloy sheet and plate of various thicknesses. Technical Memorandum (TM) NASA-TM-X-53332, NASA Marshall Space Flight Center, Huntsville, AL, United States, 1965. Public domain, Work of the US Government.
41. P. K. Liaw and W. A. Logsdon. Fatigue crack growth threshold at cryogenic temperatures: A review. *Engineering Fracture Mechanics*, 22(4):585–594, 1985.
42. Julian Rackwitz, Qin Yu, Yang Yang, Guillaume Laplanche, Easo P. George, Andrew M. Minor, and Robert O. Ritchie. Effects of cryogenic temperature and grain size on fatigue-crack propagation in the medium-entropy crconi alloy. *Acta Materialia*, 200:351–365, 2020.
43. Carlo L. Bottiglione, Alberto Carpinteri, et al. Are the paris' law parameters dependent on each material and test condition? In *19th International Conference on Fracture (ICF19)*, 2021.

44. Paul C. Okonkwo, El Manaa Barhoumi, Ikram Ben Belgacem, Ibrahim B. Mansir, Mansur Aliyu, Wilfred Emori, Paul C. Uzoma, Wesam H. Beitelmal, Ersin Akyüz, Ahmed Bahgat Radwan, and R. A. Shakoor. A focused review of the hydrogen storage tank embrittlement mechanism process. *International Journal of Hydrogen Energy*, 48(35):12935–12948, 2023.

45. Yi-Sheng Chen, Chao Huang, Pang-Yu Liu, Hung-Wei Yen, Ranming Niu, Patrick Burr, Katie L. Moore, Emilio Martínez-Pañeda, Andrej Atrens, and Julie M. Cairney. Hydrogen trapping and embrittlement in metals – a review. *International Journal of Hydrogen Energy*, 136:789–821, 2025.

46. Haiyang Yu, Andrés Díaz, Xu Lu, Binhan Sun, Yu Ding, Motomichi Koyama, Jianying He, Xiao Zhou, Abdelali Oudriss, Xavier Feaugas, and Zhiliang Zhang. Hydrogen embrittlement as a conspicuous material challenge: Comprehensive review and future directions. *Chemical Reviews*, 124(10):6271–6392, May 2024.

47. Alessandro Campari, Federico Ustolin, Antonio Alvaro, and Nicola Paltrinieri. A review on hydrogen embrittlement and risk-based inspection of hydrogen technologies. *International Journal of Hydrogen Energy*, 48(90):35316–35346, 2023.

48. Shengyu Jiang, Yuantao Xu, Ruihong Wang, Xinren Chen, Chaoshuai Guan, Yong Peng, Fuzhu Liu, Mingxu Wang, Xu Liu, Shaoyou Zhang, Genqi Tian, Shenbao Jin, Huiyuan Wang, Hiroyuki Toda, Xuejun Jin, Gang Liu, Baptiste Gault, and Jun Sun. Structurally complex phase engineering enables hydrogen-tolerant al alloys. *Nature*, 641(8062):358–364, May 2025.

49. Huan Zhao, Poulami Chakraborty, Dirk Ponge, Tilmann Hickel, Binhan Sun, Chun-Hung Wu, Baptiste Gault, and Dierk Raabe. Hydrogen trapping and embrittlement in high-strength al alloys. *Nature*, 602(7897):437–441, 2022.

50. Chris San Marchi, Martina Schwarz, and Joseph Ronevich. Effect of high-pressure hydrogen and water impurity on aluminum alloys. In *Pressure Vessels and Piping Conference, Volume 6: Materials and Fabrication*, page V006T06A089, Aug 2020.

51. Chris San Marchi, Martina Schwarz, and Joseph Ronevich. Effect of high-pressure hydrogen and water impurity on aluminum alloys. In *Proceedings of the ASME 2020 Pressure Vessels and Piping Conference (PVP2020)*, San Diego, CA, USA, 2020. ASME. Sandia National Laboratories & University of Stuttgart.

52. Suleyman Kilic, Fahrettin Ozturk, and Mehmet Fatih Demirdogen. A comprehensive literature review on friction stir welding: Process parameters, joint integrity, and mechanical properties. *Journal of Engineering Research*, 13(1):122–130, 2025.

53. Brijesh Kumar Yadav, Shailendra Singh Bhadauria, and Varun Sharma. A review on fracture and fatigue behaviour of fsw joints of al alloys. *Department of Industrial and Production Engineering, Dr B R Ambedkar National Institute of Technology, Jalandhar*, 2025. Jalandhar 144027, India.

54. R.S. Mishra and Z.Y. Ma. Friction stir welding and processing. *Materials Science and Engineering: R: Reports*, 50(1):1–78, 2005.

55. Bo Du, Zhuanping Sun, Xinqi Yang, Lei Cui, Jianling Song, and Zhongping Zhang. Characteristics of friction plug welding to 10 mm thick aa2219-t87 sheet: Weld formation, microstructure and mechanical property. *Tianjin Key Laboratory of Advanced Joining Technology, School of Materials Science and Engineering, Tianjin University*,

2015. Tianjin Long March Rocket Manufacture Co., LTD., Tianjin, China.

56. Noor Zaman Khan, Annayath Maqbool, Tariq Ahmad, Arshad Noor Siddiquee, and Zahid A. Khan. Fracture behaviour of friction stir welded dissimilar aluminium alloys. *Materials Today: Proceedings*, 37, Part 6:5653–5660, 2021.

57. Chao He, Kazuhiro Kitamura, Kun Yang, Yong-jie Liu, Qing-yuan Wang, and Qiang Chen. Very high cycle fatigue crack initiation mechanism in nugget zone of aa 7075 friction stir welded joint. *Advances in Materials Science and Engineering*, 2017:10, 2017.

58. Robert Kosturek, Tomasz Ślezak, Janusz Torzewski, Marcin Wachowski, and Lucjan Śnieżek. Study on tensile and fatigue failure in the low-hardness zone of aa2519-t62 fsw joint. *Metallurgical Research & Technology*, 119(5):502, 2022.

59. Kathryn Anderson-Wedge, G. Stubblefield, N. Zhu, B. Long, S. R. Daniewicz, P. Allison, J. Sowards, O. Rodriguez, and R. Amaro. Characterization of the evolution of 2219-t87 aluminum as a function of the friction stir welding process. *International Journal of Fatigue*, 142:105929, 2021.

60. Aviation Broker GmbH. Airbus a320 fuselage diameter and dimensions, 2025. Fuselage diameter: 3.95 m. Accessed August 2025.

61. Filippo Mazzoni, Grazia Accardo, Roberta Biga, Eugenio Brusa, Cristiana Delprete, Camilo Andrés Manrique-Escobar, and Valeria Vercella. Hydrogen storage system design: Case studies for airborne application. *To be updated*, 202X. Abstract available. Affiliation: Politecnico di Torino, Italy; Leonardo Innovation Labs & Intellectual Property, Leonardo S.p.A., Italy.

62. American Society of Mechanical Engineers. Boiler and Pressure Vessel Committee. *ASME Boiler and Pressure Vessel Code*. American Society of Mechanical Engineers, New York, 1986 ed. edition, 1986. Classification No. 621.642 AME.

63. Boyd Corporation. Technical report on friction stir welding efficiency in aerospace applications, 2024. Accessed August 2025.

64. Norman Green, Alessio Tarantino, John Turner, Harina Amer Hamzah, and Haziq Noah. Flyzero: Zero-carbon emission commercial flight study. Technical report, Aerospace Technology Institute (ATI), Martell House, University Way, Cranfield, UK, 2022. Coauthors: Alessio Tarantino (Fuel Storage Lead), John Turner (Structures Design Lead), Harina Amer Hamzah (Hydrogen Specialist), Haziq Noah (Aircraft Systems Architect). Supported by the UK Department for Business, Energy and Industrial Strategy. Contributing companies: Airbus, Rolls-Royce, GKN Aerospace, Spirit AeroSystems, Reaction Engines, and others.

65. T. Oom Ortiz de Montellano, A. Heidebrecht, and M. F. M. Hoogreef. Structural analysis of a novel integral tank concept for hydrogen storage onboard commercial aircraft. In *Proceedings of the AIAA SCITECH 2025 Forum*, 2025. AIAA Science and Technology Forum and Exposition, Article AIAA 2025-1244.

66. I. K. Giannopoulos and E. E. Theotokoglou. Liquid hydrogen storage tank loading generation for civil aircraft damage tolerance analysis. *Journal of Physics: Conference Series*, 2692:012048, 2024. 7th International Conference of Engineering Against Failure, Spetses Island, Greece, 21–23 June 2023.

67. M. I. Rosenko. Pollution from ships as a factor affecting maritime transportation effi-

ciency. *E3S Web of Conferences*, 460:06014, 2023.

68. Waruna Seneviratne, John Tomblin, and Upul Palliyaguru. Bond process qualification protocols for aircraft design and certification. Technical report, Joint Centers of Excellence for Advanced Materials, Seattle, WA, April 2016. JAMS Technical Review research report.
69. J. van Muijden, B. B. Prananta, and R. P. G. Veul. Efficient aeroelastic simulation in a parametric procedure to generate structural loads for transport aircraft. In *Proceedings of the 26th International Congress of the Aeronautical Sciences (ICAS)*, 2008.
70. Robert E. Sterrgel and Pad W. Berry. Stability and control of maneuvering high-performance aircraft. NASA Contractor Report CR-194569, The Analytic Sciences Corporation, Reading, Massachusetts, April 1977.
71. V. Viswanath, A. K. Asraff, P. Jayesh, Suresh Mathew Thomas, R. Krishnakumar, and R. Muthukumar. Structural integrity assessment of a propellant tank in presence of welding residual stresses. *Procedia Structural Integrity*, 14:442–448, 2019. SICE 2018 (2nd International Conference on Structural Integrity and Exhibition 2018).
72. P. Manikandan, T. Antony Prabhu, Sushant K. Manwatkar, G. Sudarshan Rao, S. V. S. Narayana Murty, D. Sivakumar, Bhanu Pant, and M. Mohan. Tensile and fracture properties of aluminium alloy aa2219-t87 friction stir weld joints for aerospace applications. *Metallurgical and Materials Transactions A*, 52(11):4453–4467, 2021.
73. Emad Mosayyebi, Baraa Albaghdadi, Amir Ghiasvand, John Grimaldo, and Hesamoddin Aghajani Derazkola. Investigation of the effect of loading angle on mixed-mode fatigue crack propagation of aa2024-t351 friction stir welded joint. *International Journal on Interactive Design and Manufacturing (IJIDeM)*, 18, 2023.
74. Xiushuo Zhang, Yu'e Ma, Meng Yang, Wei Huang, Yilin Peng, and Zhenhai Wang. Effects of biaxial residual stress components on mixed-mode fatigue crack propagation behavior in friction stir welded 7075-t6 aluminium alloy panel. *Theoretical and Applied Fracture Mechanics*, 121:103437, 2022.
75. R. Citarella, P. Carlone, R. Sepe, and M. Lepore. Multiple crack propagation in friction stir welded aluminium joints. In P. Iványi and B. H. V. Topping, editors, *Proceedings of the Ninth International Conference on Engineering Computational Technology*, Stirlingshire, Scotland, 2014. Civil-Comp Press. Department of Industrial Engineering, University of Salerno; Department of Chemical, Materials and Production Engineering, University of Naples Federico II.
76. M. S. Shaari, M. R. M. Akramin, A. K. Ariffin, S. Abdullah, and Masanori Kikuchi. Prediction of fatigue crack growth for semi-elliptical surface cracks using s-version fem under tension loading. *Journal of Mechanical Engineering and Sciences (JMES)*, 10(3):2375–2386, 2016. Universiti Malaysia Pahang, Malaysia.
77. Stefan Kolitsch, Hans-Peter Gänser, and Reinhard Pippan. Approximate stress intensity factor solutions for semi-elliptical cracks with large a/w and c/b under tension and bending. *Theoretical and Applied Fracture Mechanics*, 92:167–177, 2017.
78. A. O. Payne. The fatigue of aircraft structures. *Engineering Fracture Mechanics*, 8(1):157–203, 1976.
79. R. D. Keys, T. F. Kiefer, and F. R. Schwartzberg. Determination of low-temperature fatigue properties of structural metal alloys: Final report, jul. 1964 – aug. 1965. NASA

Contractor Report NASA-CR-67818 / CR-65-70, Martin Company, Denver, Colorado, United States, October 1965. Fatigue testing and determination of low-temperature properties of structural metal alloys: aluminum alloy, stainless steel, and nickel alloys.

Appendices

18 June 2025

Dear Andrea

Reference: CURES/25628/2025
Project ID: 29195
Title: Structural Concepts for Metallic LH2 Tank Designs

Thank you for your application to the Cranfield University Research Ethics System (CURES).

We are pleased to inform you your CURES application, reference CURES/25628/2025 **has been reviewed. You may now proceed with the research activities you have sought approval for.**

If you have any queries, please contact CURES Support.

We wish you every success with your project.

Regards,

CURES Team

APPENDIX B: Preliminary Design

This appendix details the preliminary design considerations for the liquid hydrogen storage tank, emphasising material selection, integration strategies, insulation concepts, and manufacturing feasibility. The content is grounded on authoritative aerospace literature and recent advances, with proposed refinements to enhance clarity, completeness, and scientific rigour. Where appropriate, tables summarise decision criteria to facilitate comprehension and future reference.

Tank Material

Selecting a suitable material for LH_2 storage tanks entails balancing extreme cryogenic performance with mechanical, thermal, and manufacturing properties. Among conventional and emerging materials, the leading candidates are austenitic stainless steels, aluminium alloys, and composite materials. Austenitic stainless steels (e.g., AISI 304L, 316L) offer robustness at cryogenic temperatures with excellent ductility and resistance to hydrogen embrittlement. Their lower thermal conductivity aids insulation, but their density imposes a weight penalty detrimental for mobile aerospace applications. Aluminium alloys, notably AA2219-T87, combine low density with adequate mechanical strength and cryogenic toughness, maintaining tensile integrity even at 20 K and exhibiting minimal hydrogen-induced degradation. Aluminium's higher thermal conductivity challenges insulation but can be compensated by advanced multilayer systems. Composite tanks, using CFRP or glass fibre laminates with metallic or polymer liners, promote weight reduction and fatigue resistance, yet introduce concerns over microcracking and permeation under thermal cycling, making their industrial readiness less mature.

Table 10: Comparison matrix for material selecction

Criterion / Property	**Steel**	**Aluminum (AA2219-T87)**	**Composites**	**Weight** (%)	**Score** Steel	**Weighted** Steel	**Score** Aluminum	**Weighted** Aluminum	**Score** Composites	**Weighted** Composites
Strength and Toughness at 20K	High	Good	High	25	4	1.00	4	1.00	5	1.25
Weight Efficiency	Low	High	Very High	25	2	0.50	4	1.00	5	1.25
Resistance to Hydrogen Embrittlement	Good	Good	Moderate	15	4	0.60	5	0.75	3	0.45
Thermal Conductivity	Low	Higher	Low to moderate	10	4	0.40	2	0.20	3	0.30
Manufacturability	Moderate	High	Moderate to Low	15	3	0.45	4	0.60	2	0.30
Cost	Low	Moderate	High	10	4	0.40	3	0.30	1	0.10
Total Score	—	—	—	100	—	**3.35**	—	**3.85**	—	**3.65**

Based on this evaluation and literature evidence, AA2219-T87 aluminium alloy is selected for the tank to optimise structural integrity, manufacturability, and weight performance in the cryogenic environment.

Tank Integration

Tank geometry and placement strongly influence aircraft performance and maintenance. LH_2 tanks are typically classified as integral or non-integral relative to the airframe.

Integral tanks serve dual roles as both hydrogen storage and structural members, offering superior mass efficiency and load transfer optimisation, particularly suited for future blended wing body (BWB) aircraft with high internal volume utilisation. However, they pose challenges in access, inspection, and require bespoke design adaptations for each aircraft configuration.

Non-integral tanks are modular units isolated from primary structure, offering maintenance ease, retrofit flexibility, and standardised designs. The trade-off includes increased structural parasitism and reduced volumetric and aerodynamic optimisation, especially for advanced airframes like BWB.

Table 11: Comparison matrix for tank integration selection

Criterion	Integral Tank	Non-Integral Tank	Weight (%)	Score Integral	Weighted Integral	Score Non-Integral	Weighted Non-Integral
Maintenance Access and Downtime	Challenging	Easy; modular and replaceable	25	1	0.25	5	1.25
Load Isolation and Structural Contribution	Direct load-bearing; highly efficient	Structurally isolated; parasitic weight	25	5	1.25	2	0.50
Mass Efficiency	Highest; integrated structure reduces weight	Lower; extra supports add weight	15	5	1.00	3	0.60
Integration with Current Aircraft	Requires redesign; less versatile	Easily retrofitted; flexible	20	2	0.40	5	1.00
Suitability for Future Configurations (BWB)	Optimal volumetric and aerodynamic synergy	Limited optimization due to modular constraints	15	4	0.60	2	0.30
Total Score	—	—	100	—	**3.00**	—	**3.65**

Considering operational flexibility and scope, the tank design adopts a non-integral configuration with bolted attachments to fuselage I-type frames. These attach points will be conceptual only, with frame sizing and bolt configuration based on analogous designs validated via FEM.

Insulation Concepts

Insulation critically governs boil-off rates and safety. The two main approaches are: Multilayer Insulation (MLI): Vacuum-based, consisting of many reflective foil layers separated by spacers inside a double-wall structure maintaining vacuum below 1 Pa, MLI minimizes conductive/radiative heat transfer, achieving heat leaks as low as 0.9 W/m^2 and boil-off near 0.20%. However, vacuum integrity risk necessitates robust structures and backup foam layers to maintain insulation if vacuum is lost. Spray-On Foam Insulation (SOFI): Polyurethane foam applied on surfaces offers ease and weight benefits but is prone to microcracks on thermal cycling, has higher thermal conductivity, and results in about 43 W/m^2 heat leak and 12% daily boil-off, less suited for aviation LH_2 storage.

Table 12: Comparison matrix for insulation systems

Criterion	Value MLI	Value SOFI	Weight (%)	Score MLI	Weighted MLI	Score SOFI	Weighted SOFI
Thermal Conductivity / Heat Leak (W/m^2)	0.9	43	30	5	1.50	2	0.60
Daily Boil-off (%)	0.20	12	30	5	1.50	2	0.60
Vacuum Dependency	High	None	15	2	0.30	5	0.75
Weight Penalty	Moderate (double-wall)	Low	10	3	0.30	4	0.40
Operational Safety (Boil-off/Pressure Control)	High (minimal boil-off)	Medium (higher boil-off)	10	5	0.50	3	0.30
Durability Under Thermal Cycling	High; stable with vacuum	Low; prone to microcracking	5	4	0.20	2	0.10
Maintenance Complexity	Medium; vacuum maintenance	Low; easier inspection	5	3	0.15	4	0.20
Total Weighted Score	—	—	100	—	4.45	—	2.95

Given the critical requirement to minimise boil-off and maximise operational safety, MLI is selected as the primary insulation method. Secondary foam layers will be considered for vacuum breach mitigation.

Manufacturing Feasibility

Manufacturing techniques directly impact tank performance via material properties and structural integrity.

Cylindrical Zone: Deep drawing is employed to form seamless cylindrical shells with uniform wall thickness, crucial for fatigue resistance. The process induces strain hardening, enhancing yield strength but requiring post-forming heat treatment to relieve residual stresses and prevent fatigue crack initiation. For very large tanks, rolling plates into cylindrical shells followed by high-integrity welding is an option, though it introduces anisotropy and tensile residual stresses if not controlled.

Table 13: Comparison matrix for cylindrical zone manufacturing

Criterion	Weight (%)	Score – Rolling	Weighted – Rolling	Score – Deep Drawing	Weighted – Deep Drawing
Residual Stress Control	25	2	0.50	4	1.00
Grain Refinement Quality	20	3	0.60	4	0.80
Fatigue Life Potential	25	3	0.75	4	1.00
Manufacturability	15	3	0.45	5	0.75
Suitability for LH Cylinders	15	3	0.45	5	0.75
Total Score	100	—	2.75	—	4.30

Dome Ends: Spin forming (spinning) allows symmetric, robust dome production, with hot spinning preferred for thicker domes to maximise deformation without cracking. Hydroforming offers superior precision and uniform thickness with lower residual stresses, beneficial for complex dome geometries and specially alloys, enhancing fatigue life.

Table 14: Comparison matrix for dome ends manufacturing

Criterion	Weight (%)	Score – Spinning	Weighted – Spinning	Score – Hydroforming	Weighted – Hydroforming
Residual Stress Control	25	4	1.00	5	1.25
Grain Refinement Quality	20	4	0.80	5	1.00
Fatigue Life Potential	25	4	1.00	5	1.25
Manufacturability	15	4	0.60	4	0.60
Suitability for LH Domes	15	4	0.60	5	0.75
Total Score	100	—	4.00	—	4.85

Attachment between Sections: Friction Stir Welding (FSW) is selected for joints due to its solid-state nature, resulting in refined microstructure, high tensile strength, and superior fatigue resistance with minimal defects. While Tungsten Inert Gas (TIG) welding is common, it is more prone to defects and induces coarser grain zones and residual stresses, which may limit fatigue performance.

Table 15: Comparison matrix for aluminum joining

Criterion	Weight (%)	Score – FSW	Weighted – FSW	Score – TIG	Weighted – TIG
Residual Stress Control	25	5	1.25	2	0.50
Grain Refinement Quality	20	5	1.00	2	0.40
Fatigue Life Potential	25	5	1.25	2	0.50
Manufacturability	15	4	0.60	3	0.45
Suitability for LH Joints	15	5	0.75	3	0.45
Total Score	100	—	4.85	—	2.30

Attachment to the Fuselage

As previously discussed, the cylindrical section and the domes will be joined using friction stir welding (FSW) in combination with I-section circular beams. This joint configuration presents some particular considerations. The fuselage frames have a greater thickness than the tank components (both the cylindrical shell and the domes). Since FSW requires consistent thickness at the welding interface to ensure optimal joint quality, the frame geometry will incorporate a gradual thickness reduction in the welding zone to match the tank wall thickness.

Furthermore, the edge of the dome is structurally critical due to the presence of geometric discontinuities, which can concentrate stresses and accelerate fatigue damage. Welding the frame directly at the dome's termination would therefore increase stress concentrations and reduce fatigue life. To mitigate this effect, the frames are positioned slightly inward from the dome edge, closer to the cylindrical mid-section, where stress distribution is more uniform.

These frames serve as the attachment interface for the I-section fuselage frames. The connection between the tank frames and fuselage structure will be realised through bolted joints to ensure structural integrity under operational loads. The detailed design of this bolted attachment lies outside the scope of the present thesis but is acknowledged as a critical step in the integration process.

Summary of Preliminary Design Decisions:

Table 16: Summary of Preliminary Design Decisions

Feature	Design Decision
Tank Material	Aluminum Alloy AA2219-T87
Integration	Non-integral, bolted frames
Insulation	Multilayer Insulation (MLI)
Manufacturing	Cylindrical: Deep drawing
	Domes: Hydroforming
	Joints: Friction Stir Welding (FSW)

APPENDIX C: Tank geometry impact

To compare and analyse the impact of integrating a hydrogen fuel tank into a tube-wing aircraft configuration, specifically the Airbus A320, a detailed study has been conducted. This study contrasts the performance and design implications of using kerosene versus hydrogen as the primary aviation fuel.

The tank diameter for this analysis is based on the Airbus A320 fuselage diameter, which is 3.95 metres. To allow for tolerance and sufficient space for attachment and integration between the tank and the fuselage, the tank diameter has been fixed at 3 metres. This choice ensures a practical balance between accommodating the tank and maintaining structural and aerodynamic integrity.

The baseline for comparison is the original A320 configuration, focusing on parameters such as range, kerosene fuel volume, and passenger seating capacity per row. Given the fundamental differences between kerosene and hydrogen in terms of density and energy content, an equivalence analysis has been performed. The key fuel properties considered are summarised in Table 17.

Table 17: Comparison of Kerosene and Hydrogen energy properties

Fuel	Density (kg/L)	Energy per Mass (MJ/kg)	Energy per Volume (MJ/L)	Energy Density Ratio Mass	Energy Density Ratio Volume
Kerosene	0.80	43	35	1.0	1.0
Hydrogen	0.07	141	8.5	3.3 × kerosene	0.24 × kerosene

Based on these values, hydrogen has approximately 3.3 times higher gravimetric energy density than kerosene but only about 24% of its volumetric energy density. This volumetric limitation necessitates larger storage volumes for hydrogen to provide the same energy content as kerosene.

Tank Volume Calculations

To calculate the equivalent energy storage for hydrogen in the A320, the tank volume must increase correspondingly. Further analysis was conducted considering tank volumes composed of a cylindrical section with hemispherical domes at both ends:

$$V_{\text{domes}} = \frac{4}{3}\pi r^3$$

$$V_{\text{cylinder}} = L\pi r^2$$

$$V_{\text{total}} = V_{\text{domes}} + V_{\text{cylinder}}$$

Various tank lengths were evaluated to calculate the total hydrogen fuel volume, the corresponding range, and the reduction in passenger rows and total passengers. The range was scaled according to the total tank volume, the A320 range, and the energy density ratio between hydrogen and kerosene:

$$\text{Range} = \frac{V_{\text{total}} \times \text{A320 Range} \times \text{Energy Density Ratio}_{\text{Mass}}}{\text{A320 Kerosene Volume}}$$

Table 18: Evaluation of tank length for range and passenger reduction

L_{cyl} (m)	β	L_{tot} (m)	V_{cyl} (m^3)	V_{tot} (m^3)	Range (km)	Rows	Total Pax
1	0.75	4	7.07	21.21	1409.39	30	134
2	0.60	5	14.14	28.27	1879.18	38	125
3	0.50	6	21.21	35.34	2348.98	45	119
4	0.43	7	28.27	42.41	2818.77	53	112
5	0.38	8	35.34	49.48	3288.57	60	104
6	0.33	9	42.41	56.55	3758.37	68	97
7	0.30	10	49.48	63.62	4228.16	75	89

The study found that a 5-metre cylindrical length (with 3-metre diameter domes) offered a reasonable compromise. Such a configuration provides a range of approximately 1880 km, which is about 60% of the original A320 range, classifying it more as a regional aircraft. The passenger capacity reduction is limited to 38 seats, maintaining a practical balance between energy storage and meaningful operational capability.

APPENDIX D: Global FEM

This appendix presents a detailed account of the global finite element analysis conducted as part of the structural validation process, serving as a foundational step before proceeding to more detailed investigations. The purpose of this analysis is to verify the global structural behaviour under relevant loading conditions and to ensure the model's adequacy for subsequent focused analyses.

The geometric model was developed based on the structural design, with a focus on simplicity and computational efficiency. Although the structure's geometry is straightforward enough to be directly generated within the Abaqus interface, the model was primarily created using 3D Experience software. The components—domes, cylindrical sections, and frames—were modelled separately to allow refined control over their definition. To reduce model complexity, only the lower flange of the frames was included, providing a reasonable simplification that does not compromise the accuracy of the global response.

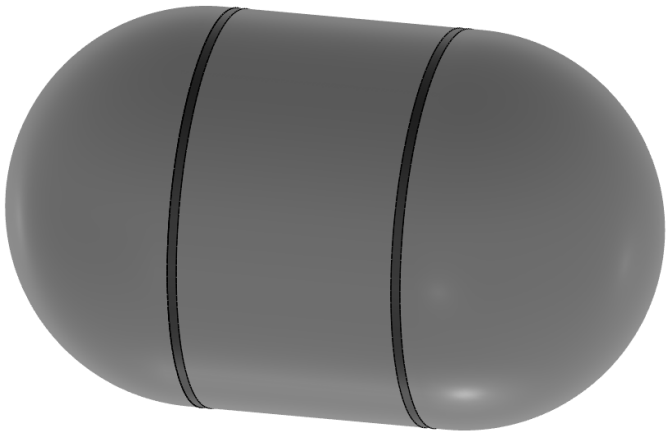
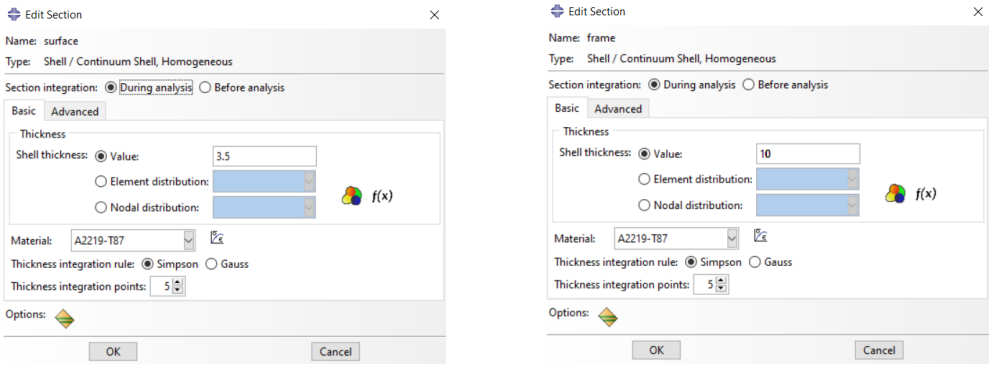


Figure 25: 3D geometry of the tank in 3D Experience software.

To optimise computational resources, a surface-based representation of the geometry was employed instead of solid modelling, with the assigned shell thicknesses accounting for the structural element dimensions. The geometry was exported as a STEP (`.stp`) file and imported into Abaqus. Material properties were assigned with particular attention: the cylindrical and dome sections were modelled with a thickness of 3.5 mm, while the frames were assigned a thickness of 10 mm, reflecting their structural role.



a) Tank surface b) Frame

Figure 26: Property definition

Upon assembly, the separately modelled parts required the definition of interactions to simulate the connections. A "tie" constraint was applied between interfaces, reflecting welded joint behaviour typical in such assemblies. This choice is justified as it prevents relative motion or separation, accurately representing the rigid connection expected in the physical structure.

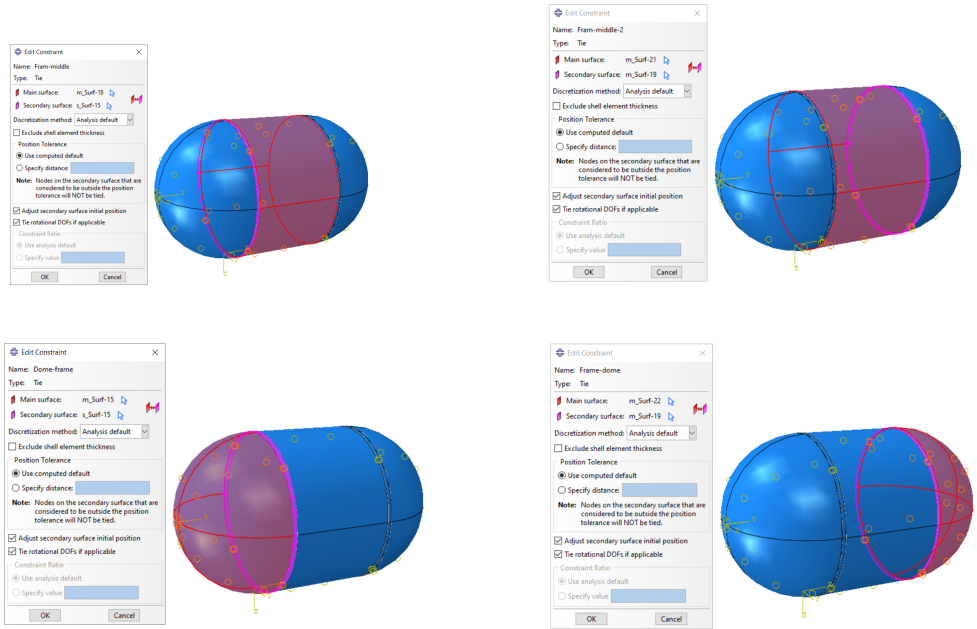


Figure 27: Tie defintion for welded joints

Hexahedral elements were selected for meshing, chosen for their superior convergence characteristics and accuracy in stress predictions compared to tetrahedral elements, especially for structural shell models. In the case of the dome geometries, partitioning was applied strategically to accommodate the sweep meshing method, facilitating a high-quality element distribution. A mesh convergence study was conducted to identify an optimal mesh size at which the maximum stress values stabilised. This ensured result accuracy while maintaining computational efficiency. Mesh quality was verified, with aspect ratios kept below 2 to avoid distorted elements that could impact result fidelity.

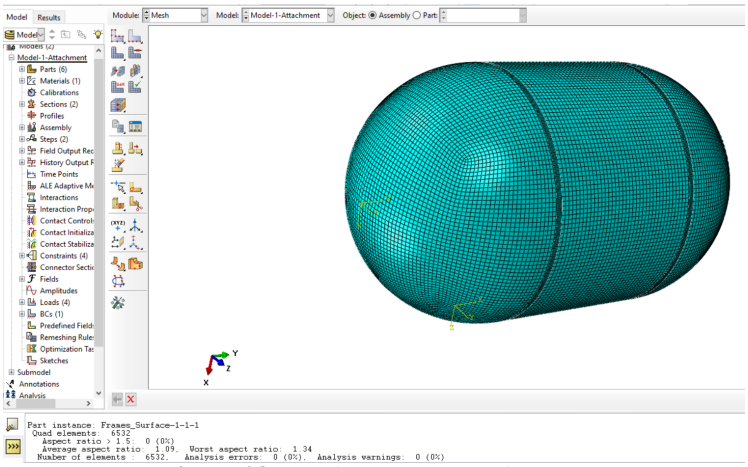


Figure 28: Maximum aspect ratio: 1.34

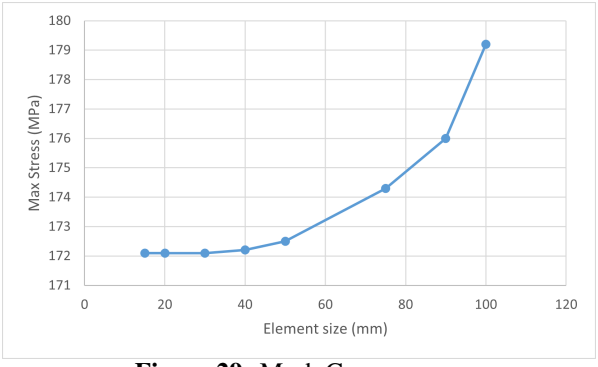


Figure 29: Mesh Convergence

Boundary conditions were applied by fully constraining the frame surfaces (fixing translations and rotations), simulating the support conditions appropriately. Multiple constraint configurations were tested to confirm that these restraints did not induce unrealistic stiffness or artificial stress concentrations, thereby preserving physical validity.

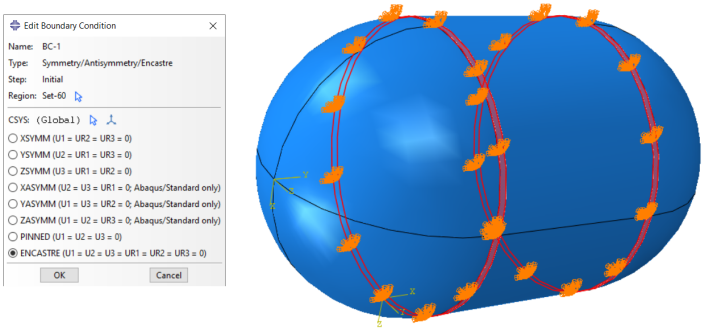


Figure 30: Mesh for Global FEM analysis

The applied load types:

1. **Static pressure loading:** representing tank pressurization with an internal pressure of 0.45 MPa applied uniformly on the internal surface.

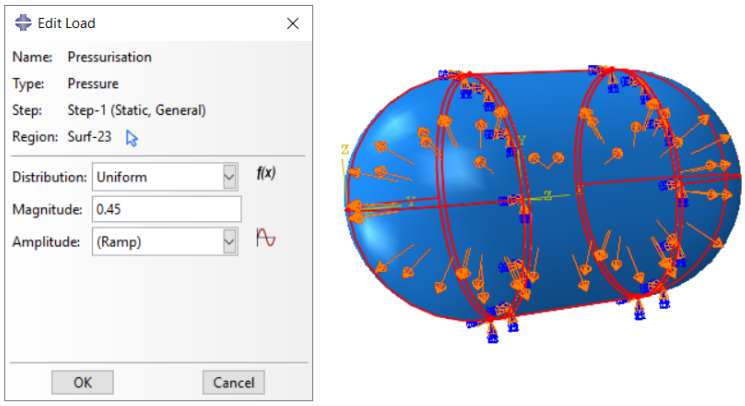


Figure 31: Pressurisation Load

2. **Hydrostatic load cases:** simulating inertial effects under accelerations relevant to operational scenarios. Depending on severe or extreme manoeuvres. Longitudinal, vertical, and lateral accelerations were individually applied. A hydrostatic pressure distribution following the appropriate formulation was imposed on the inner skin. This was coupled with an analytical field definition and a dedicated coordinate system to accurately represent variable pressure distribution.

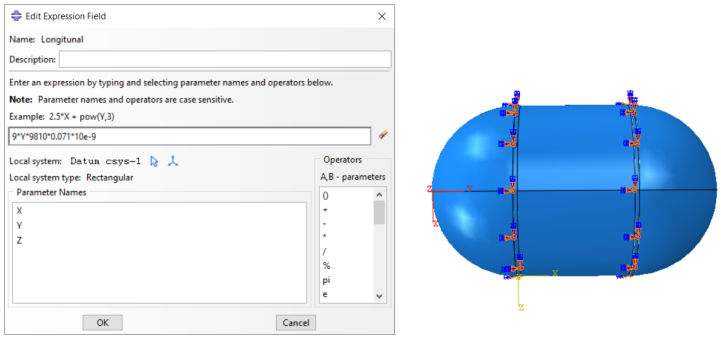


Figure 32: Analytical field defintion for longitudinal 9g intertial load

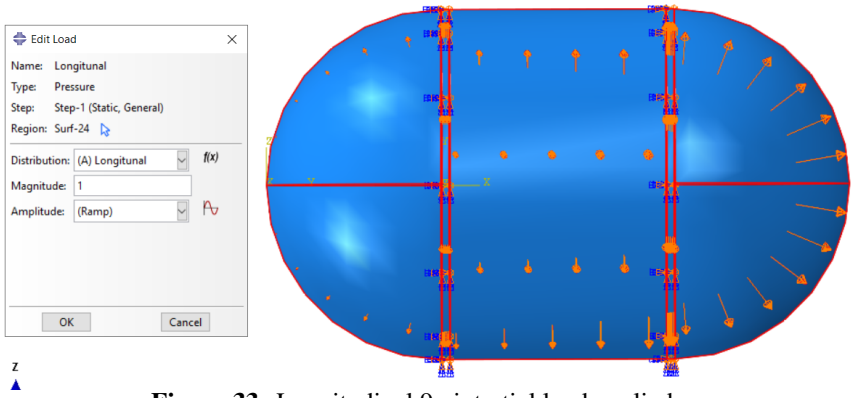


Figure 33: Longitudinal 9g intertial load applied

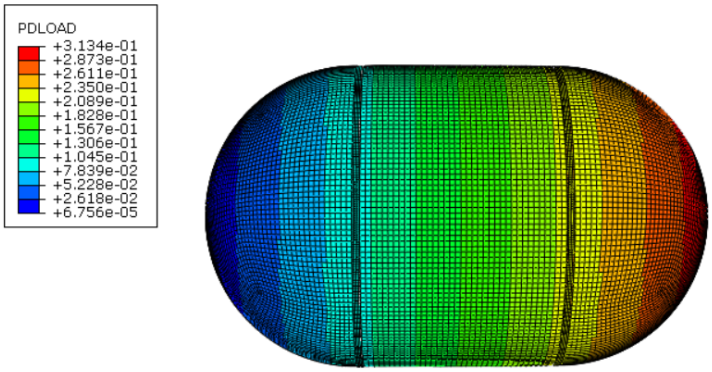
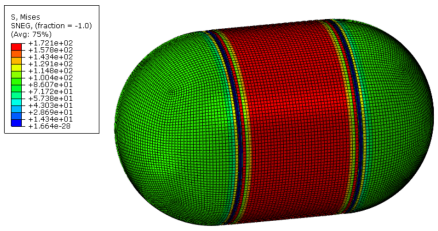
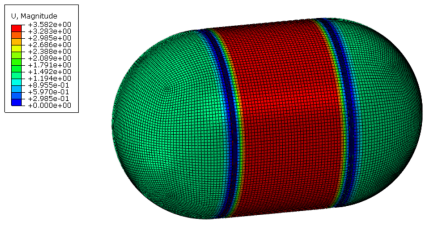


Figure 34: Longitudinal 9g intertial load: pressure load (PDLOAD)

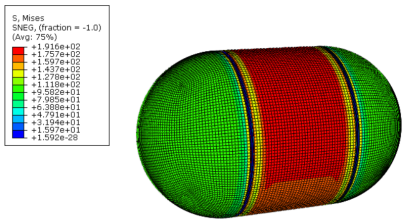
The mentioned cases are analysed, and shown in the following pictures:

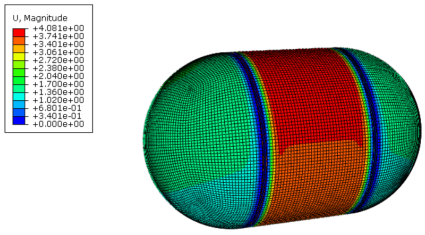




a) Max VM stress: 172.10 MPa b) Max deformation: 3.58 mm

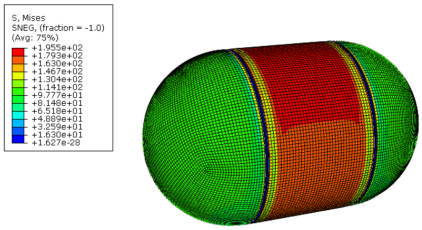
Figure 35: Results under 1 load case

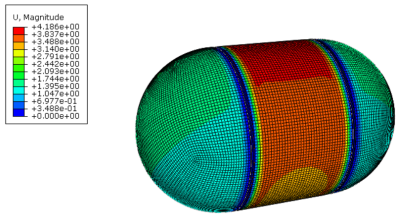




a) Max VM stress: 191.6 MPa b) Max deformation: 4.08 mm

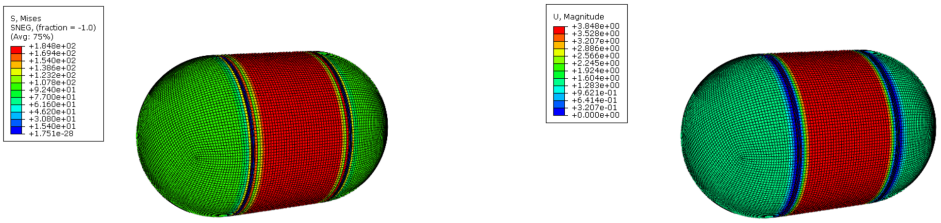
Figure 36: Results under 2a load case





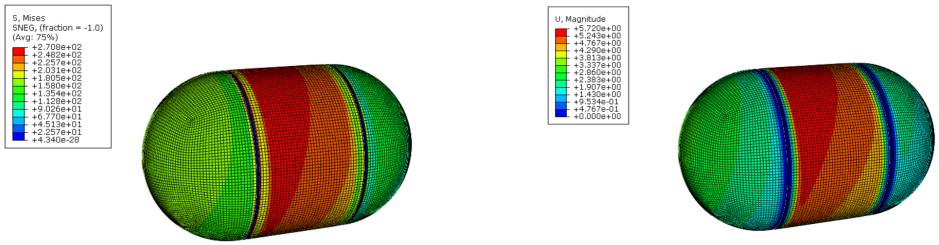
a) Max VM stress: 195.5 MPa b) Max deformation: 4.18 mm

Figure 37: Results under 2b load case



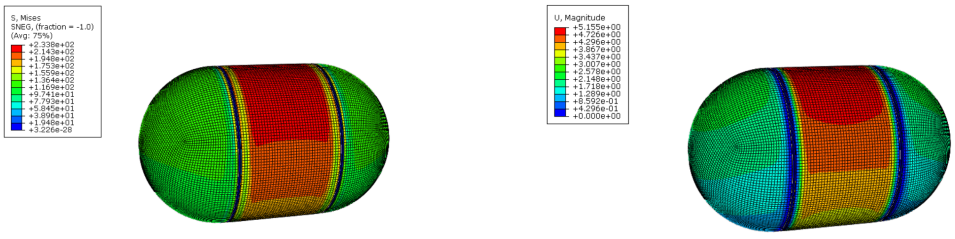
a) Max VM stress: 184.8 MPa b) Max deformation: 3.85 mm

Figure 38: Results under 2c load case



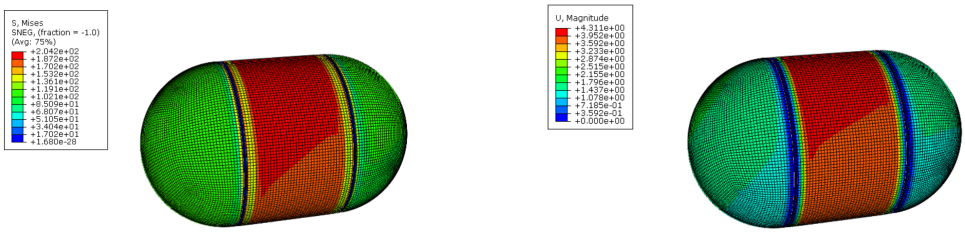
a) Max VM stress: 270.8 MPa b) Max deformation: 5.72 mm

Figure 39: Results under 3a load case



a) Max VM stress: 233.8 MPa b) Max deformation: 5.16 mm

Figure 40: Results under 3b load case



a) Max VM stress: 204.2 MPa b) Max deformation: 4.31 mm

Figure 41: Results under 3c load case

Results from these analyses are summarised in the table below, showing maximum stress and deformation values per load case, providing clear insights into structural performance and critical loading conditions.

Table 19: Global FEM analysis results: Von Mises stress, deformation and safety factor for different load cases

Load case	Maximum VM stress (MPa)	Maximum deformation (mm)	SF
1	172.1	3.58	1.98
2a	191.6	4.08	1.78
2b	195.5	4.18	1.74
2c	184.8	3.85	1.84
3a	270.8	5.72	1.26
3b	233.8	5.16	1.45
3c	204.2	4.31	1.67

As can be observed from the results, all calculated safety factors exceed unity, which confirms that the tank structure remains within the allowable design limits. This outcome indicates that, under the applied loading conditions, the stresses experienced by the tank do not surpass the permissible material strength, thereby ensuring structural integrity and compliance with the established safety requirements.

APPENDIX E: Detailed FEM

This appendix provides a comprehensive description of the detailed finite element analysis conducted to investigate the behaviour of cracks in the welded joint regions of the structure. This analysis builds upon the global model, narrowing focus to critical areas where cracks may initiate and propagate, with particular emphasis on the evaluation of the Stress Intensity Factor (SIF).

The detailed model was developed as a submodel extracted from the global Abaqus model, specifically targeting the welded joint area. Submodelling is a technique in Abaqus that allows the extraction of detailed stress and strain information in a localised region using boundary conditions transferred from the global model, ensuring consistency between global and local responses while managing computational cost effectively. This method requires careful alignment of the submodel with the global geometry to ensure accurate information transfer.

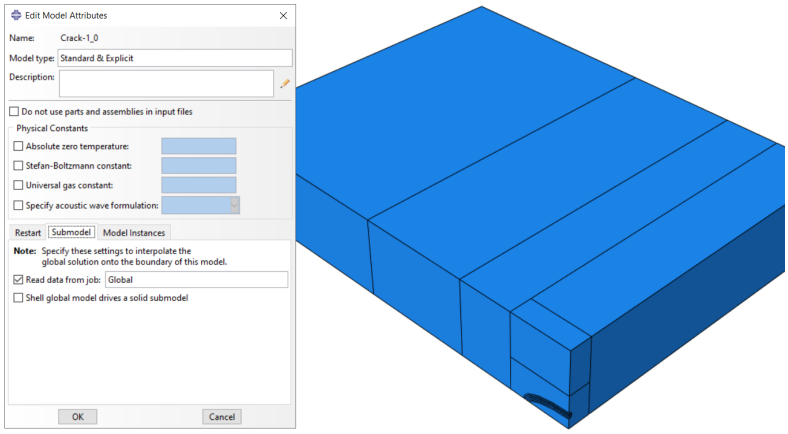


Figure 42: Submodel from general model

The submodel geometry focussed on the welded joint, which was isolated and converted into a three-dimensional solid model with a thickness of 3.5 mm, matching the shell thickness used in the global model. This consistency in thickness between the global shell model and the detailed 3D submodel prevents errors at the interface and ensures compatible boundary conditions. The welded zone was subdivided into distinct microstructural regions known to have different mechanical properties, namely:

- Nugget Zone (NZ)
- Thermo-Mechanically Affected Zone (TMAZ)
- Heat-Affected Zone (HAZ)
- Base Material (BM)

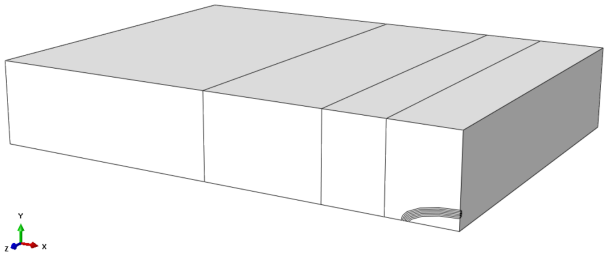


Figure 43: Model partition for different FSW zones

This subdivision reflects the real variations in microstructure and material behaviour observed in friction stir welded joints, allowing a more accurate fracture assessment. To represent cracks, the crack size was initially defined by specifying the crack face within the submodel. The crack tip region was meshed with an increased level of detail by generating contours around the crack tip. The geometry near the crack tip was partitioned and meshed using the sweep tool to facilitate a high-quality, structured mesh that is critical for accurate fracture mechanics calculations.

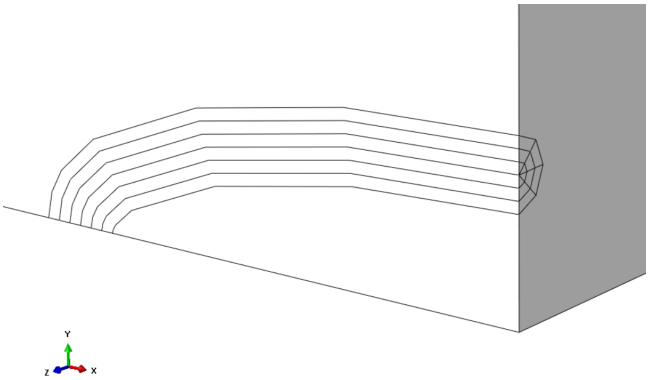


Figure 44: Division of crack to facilitate the meshing

Material properties were assigned distinctly for each microstructural zone, reflecting their specific elastic and plastic behaviours documented in the literature for friction stir welded joints.

Table 20: Mechanical properties across different weld zones

Zone	E (GPa)	Poisson (–)	J (kJ/m^2)	Max Principal Stress (MPa)	Distance from centre (mm)
NZ	70	0.33	28	295	2.75
TMAZ	70	0.33	22.5	250	5.25
HAZ	72	0.33	32	292.5	10.25
BM	72	0.33	40	477.5	—

In assembling the submodel, a local coordinate system was defined to ensure proper alignment with the global tank model. This alignment was confirmed by placing the submodel within the global assembly, allowing the boundary conditions and load transfer to be correctly applied.

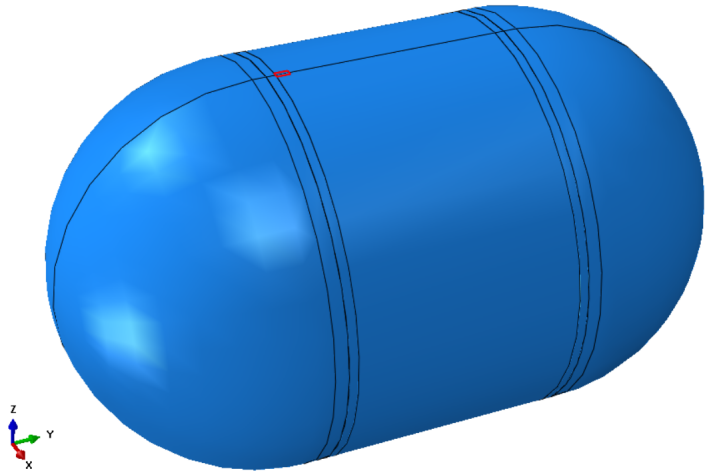
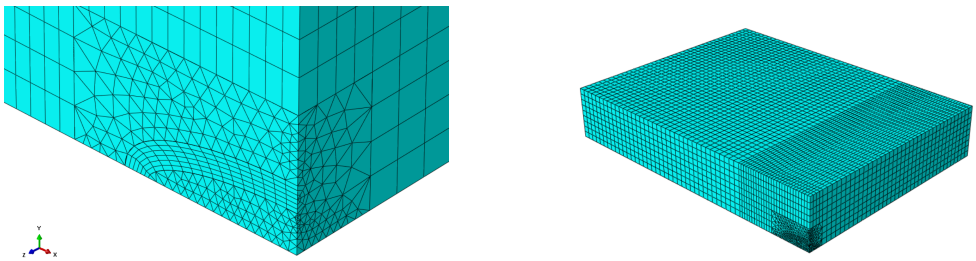


Figure 45: Submodel from general model

Hexahedral (hex) elements were used for most of the model, while the crack tip and its immediate vicinity were meshed with tetrahedral elements to accurately capture singularity and stress gradients during contour integral evaluations in Abaqus. The surrounding region employed free meshing to balance mesh quality with computational efficiency.



a) Detailed mesh of the crack b) Global mesh of the model

Figure 46: Submodel meshing

The crack definition within Abaqus employed the contour integral method, a robust technique to compute stress intensity factors that leverages a set of integral contours around the crack tip to capture the singular stress field without requiring extrapolation. The crack front and propagation direction were explicitly defined to guide the calculation of K_I and facilitate potential crack growth analyses.

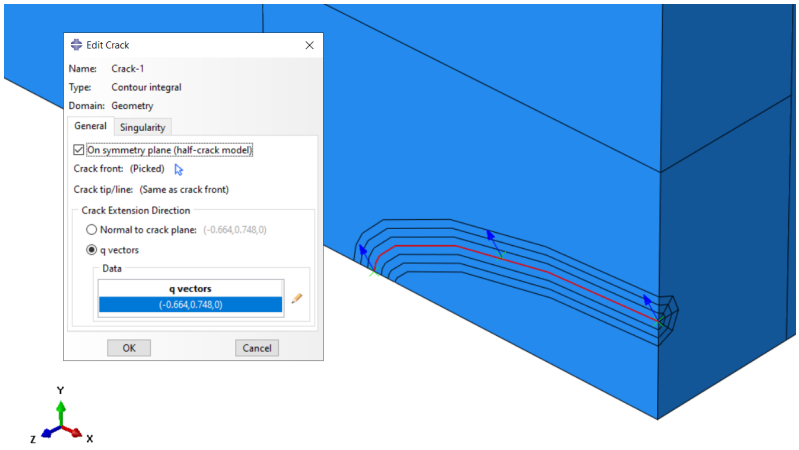


Figure 47: Contour integral: crack direction definition

Boundary conditions were applied to reflect symmetry and continuity. The crack face lying on a symmetry plane was constrained in translation perpendicular to the plane, reflecting realistic structural constraints and reducing the computational domain. At the interfaces connecting the submodel to the tank model (the lateral and parallel faces adjacent to the crack), submodel constraints were imposed to restrict unwanted rigid body motions and ensure displacement compatibility with the global model. The internal surface of the model was subjected to a uniform internal pressure of 0.45 MPa, consistent with the pressurisation load used in the global analysis.

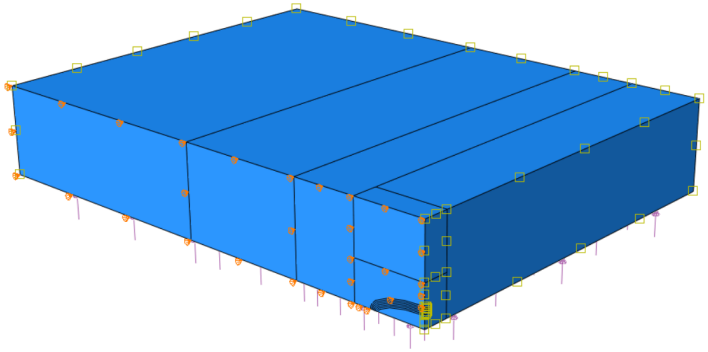


Figure 48: Boundary conditions for submodel (yellow)

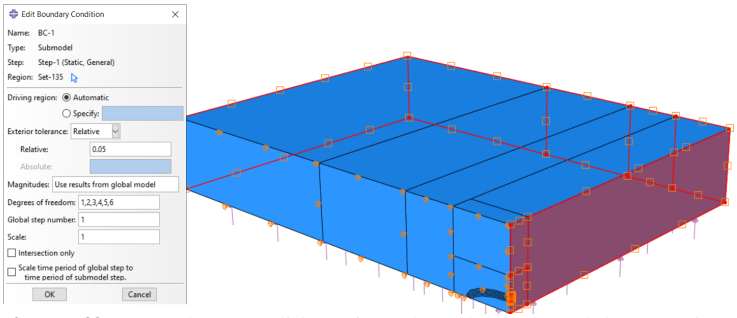


Figure 49: Boundary conditions for submodel: submodel constraints

Results from the analysis revealed that the maximum K_I values coincided spatially with the locations of maximum stress, validating the accuracy of the modelling approach. The variation of K_I along the crack front was examined across different contour layers, demonstrating the expected stability and convergence of the fracture parameter.

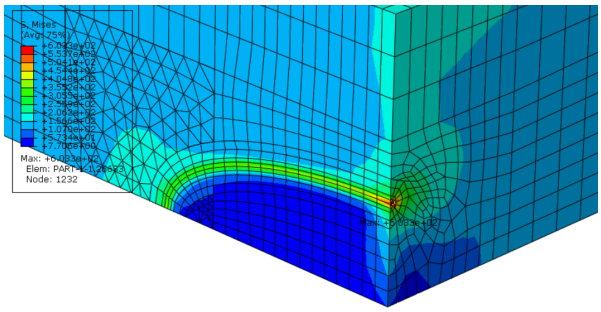


Figure 50: Submodel results: Stress (VM)

K FACTOR ESTIMATES

CRACK NAME	CRACKFRONT NODE SET		CONTOURS 1	2	3
H-OUTPUT-2_CRACK-1					
	-18-	K1:	559.1	581.7	600.0
		K2:	0.000	0.000	0.000
		K3:	0.000	0.000	0.000
	MTS	DIRECTION (DEG):	0.000	0.000	0.000
		J from Ks:	3.979	4.307	4.583
	-29-	K1:	542.3	547.2	544.2
		K2:	0.000	0.000	0.000
		K3:	0.000	0.000	0.000
	MTS	DIRECTION (DEG):	0.000	0.000	0.000
		J from Ks:	3.744	3.811	3.770
	-31-	K1:	533.1	539.6	538.0
		K2:	0.000	0.000	0.000
		K3:	0.000	0.000	0.000
	MTS	DIRECTION (DEG):	0.000	0.000	0.000
		J from Ks:	3.618	3.706	3.684
	-32-	K1:	528.6	534.9	533.4
		K2:	0.000	0.000	0.000
		K3:	0.000	0.000	0.000
	MTS	DIRECTION (DEG):	0.000	0.000	0.000
		J from Ks:	3.557	3.643	3.621

Figure 51: K_I value along the crack contour and crack length

The analysis was repeated for several crack lengths, and the resulting K_I versus crack length relationship was plotted to provide insight into the fracture behaviour under increasing crack sizes.

Crack-1			
a	=	0,75	
b	=	2,5	
Ang	=	0,75	
Contour	Angle	KI	Units (MPa√mm
1	90	279,5	8,84
2	89,25	264	8,35
3	88,5	259,5	8,21
4	87,75	259,2	8,20
5	87	257,5	8,14
6	86,25	256,6	8,11
7	85,5	255,1	8,07
8	84,75	253,9	8,03
9	84	252,6	7,99
10	83,25	251,4	7,95
11	82,5	250,1	7,91
12	81,75	248,8	7,87
13	81	247,6	7,83
14	80,25	246,3	7,79
15	79,5	245	7,75
16	78,75	243,5	7,70
17	78	242,4	7,66
18	77,25	241,1	7,62
19	76,5	239,7	7,58
20	75,75	238,4	7,54
21	75	237	7,49
22	74,25	235,7	7,45
23	73,5	234,2	7,41
24	72,75	232,9	7,36
25	72	231,4	7,32
26	71,25	229,8	7,27

Crack-2			
a	=	1,75	
b	=	4,375	
Crack1	=	0,9	
Contour	Angle	KI	Units (MPa√mm
1	90	380,9	12,04
2	89,1	361,8	11,44
3	88,2	355,6	11,24
4	87,3	354,2	11,20
5	86,4	350,8	11,09
6	85,5	348,5	11,02
7	84,6	345,8	10,93
8	83,7	343,3	10,86
9	82,8	340,4	10,76
10	81,9	337,5	10,67
11	81	334,4	10,57
12	80,1	331,1	10,47
13	79,2	327,7	10,36
14	78,3	324,1	10,25
15	77,4	320,6	10,14
16	76,5	317,3	10,03
17	75,6	311,9	9,86
18	74,7	312	9,87
19	73,8	310,1	9,81
20	72,9	308,5	9,75
21	72	306,6	9,69
22	71,1	304,9	9,64
23	70,2	303	9,58
24	69,3	301,1	9,52
25	68,4	299,1	9,46
26	67,5	297,1	9,39

Crack-3			
a	=	2,62	
b	=	5,25	
Crack1	=	1,666667	
Contour	Angle	KI	Units (MPa√mm
1	90,0	581,7	18,39
2	88,3	547,2	17,30
3	86,7	534,9	16,91
4	85,0	528	16,70
5	83,3	523,8	16,56
6	81,7	518,6	16,40
7	80,0	514	16,25
8	78,3	508,5	16,08
9	76,7	503,7	15,93
10	75,0	498,6	15,77
11	73,3	493,6	15,61
12	71,7	488	15,43
13	70,0	483,4	15,29
14	68,3	476,4	15,06
15	66,7	469,7	14,85
16	65,0	463,6	14,66
17	63,3	457,2	14,46
18	61,7	444,6	14,06
19	60,0	437	13,82
20	58,3	425,2	13,44
21	56,7	419,6	13,27
22	55,0	414,2	13,10
23	53,3	406,1	12,84
24	51,7	397,8	12,58
25	50,0	395,6	12,51
26	48,3	397,3	12,56

Crack-4			
a	=	2,9	
b	=	5,8	
Crack1	=	1,551724	
Contour	Angle	KI	Units (MPa√mm
1	90,0	794,8	25,13
2	88,4	746,6	23,61
3	86,9	710,9	22,48
4	85,3	686,8	21,72
5	83,8	665,4	21,04
6	82,2	647,6	20,48
7	80,7	630,2	19,93
8	79,1	615,5	19,46
9	77,6	602,3	19,04
10	76,0	592,7	18,74
11	74,5	581,6	18,39
12	72,9	575,3	18,19
13	71,4	567,2	17,93
14	69,8	560,8	17,73
15	68,3	553,7	17,51
16	66,7	546,9	17,29
17	65,2	539,7	17,07
18	63,6	532,9	16,85
19	62,1	526,5	16,65
20	60,5	519,5	16,43
21	59,0	511,1	16,16
22	57,4	505,4	15,98
23	55,9	500,2	15,82
24	54,3	500	15,81
25	52,8	485,9	15,36
26	51,2	489	15,46

Figure 52: Collected K_I values for four different cracks

This is the final graph that shows KI vs. crack length along the tank's thickness.

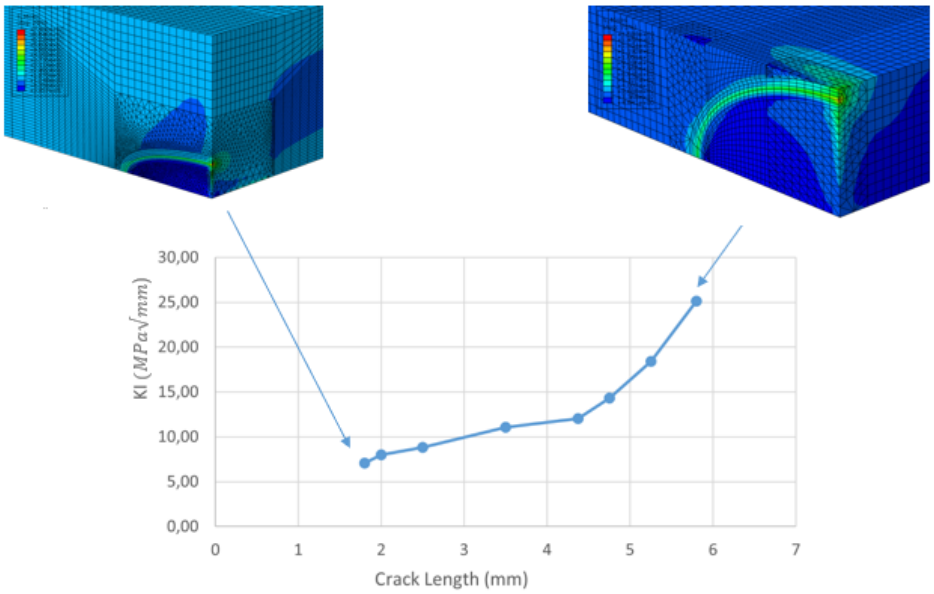


Figure 53: K_I vs a (crack length) graph

Appendix F: MATLAB Script for S-N Data Processing

```
% Experimental data from Paris' Law
DeltaK = [8.837665797, 8.965052557, 9.068282737, 9.22536103,
 ↪  9.331588593, 9.493227797, 9.630063876, 9.740951484, 9.88135827,
 ↪  9.995139465, ...
10.16827251, 10.31483874, 10.46351758, 10.61433948, 10.76733535,
 ↪  10.95384416, 11.07997474, 11.23968231, 11.33660971, 11.56603673,
 ↪  ...
11.73275043, 11.97019443, 12.14273369, 12.24744871, 12.42398433,
 ↪  12.63918917, 12.85812172, 13.26939483, 13.46066086, 13.69382271,
 ↪  ...
13.93102334, 14.09143534, 14.37661372, 14.58383928, 14.83645652,
 ↪  15.09344953, 15.22361059, 15.44304482, 15.665642, 15.98267871, ...
16.16671498, 16.35287037, 16.58858184, 16.87592468, 17.21745475,
 ↪  17.51569075, 17.81909272, 18.17971035, 18.49461428, 18.81497289];
 ↪  % K (MPa·sqrt(m))
dadN = [0.0003359, 0.000360124, 0.000402567, 0.000450014, 0.000482467,
 ↪  0.000489233, 0.000489233, 0.000524515, 0.000562341, 0.000602895,
 ↪  ...
0.000655439, 0.000702707, 0.000742964, 0.000785527, 0.000842177,
 ↪  0.000890424, 0.000928415, 0.000954638, 0.001023483, 0.001097293,
 ↪  ...
0.001128286, 0.001128286, 0.001226619, 0.001352223, 0.001409917,
 ↪  0.001470072, 0.001554291, 0.00168975, 0.001786554, 0.001837016,
 ↪  ...
0.001915394, 0.002025124, 0.00214114, 0.002263803, 0.002360391,
 ↪  0.002461099, 0.002566104, 0.002638584, 0.002751162, 0.002868543,
 ↪  ...
0.002949566, 0.003075411, 0.003162278, 0.00334344, 0.003534981,
 ↪  0.003634828, 0.003789911, 0.003951611, 0.004177993, 0.004417345];
 ↪  % da/dN (mm/cycle)

% Logarithmic transformation
logDeltaK = log10(DeltaK);
logdadN = log10(dadN);

% Linear fit (log-log): log(da/dN) = log(C) + m * log(K)
p = polyfit(logDeltaK, logdadN, 1);
m = p(1);                % Slope = Paris exponent
logC = p(2);
C = 10^logC;             % Paris Constant

% Display results
fprintf('Exponent m: %.4f and Constant C: %.3e\n', m, C)
```

Appendix G: MATLAB Script for Crack Growth Calculations

```
%% ================= m =================
% NZ
m_nz = 3.3040; C_nz = (3.067e-7);
a0_nz = 0.2; af_nz = 2.75; da_nz = 1e-7;
a_vector_KI_nz = [1.5, 2, 2.5, 3.5];
KI_vector_nz = [7.07, 7.98, 8.84, 11.08];
a_vals_nz = a0_nz:da_nz:af_nz;
KI_interp_nz = interp1(a_vector_KI_nz, KI_vector_nz, a_vals_nz,
 ↪  'spline', 'extrap');
N_nz = zeros(size(a_vals_nz));
for i = 2:length(a_vals_nz)
    KI = KI_interp_nz(i-1);
    dN = da_nz / (C_nz * KI^m_nz);
    N_nz(i) = N_nz(i-1) + dN;
end

% TMAZ
m_tmaz = 3.0818; C_tmaz = (8.678e-7);
a0_tmaz = 2.75; af_tmaz = 5.25; da_tmaz = 1e-3;
a_vector_KI_tmaz = [2.5, 3.5, 4.375, 4.75, 5.25];
KI_vector_tmaz = [8.84, 11.08, 12.04, 14.30, 18.39];
a_vals_tmaz = a0_tmaz:da_tmaz:af_tmaz;
KI_interp_tmaz = interp1(a_vector_KI_tmaz, KI_vector_tmaz,
 ↪  a_vals_tmaz, 'spline', 'extrap');
N_tmaz = zeros(size(a_vals_tmaz));
for i = 2:length(a_vals_tmaz)
    KI = KI_interp_tmaz(i-1);
    dN = da_tmaz / (C_tmaz * KI^m_tmaz);
    N_tmaz(i) = N_tmaz(i-1) + dN;
end
N_tmaz = N_tmaz + N_nz(end);

% HAZ
m_haz = 3.0818; C_haz = (8.678e-7);
a0_haz = 5.25; af_haz = 10; da_haz = 1e-3;
a_vector_KI_haz = [5.25, 5.8, 6];
KI_vector_haz = [18.39, 25.13, 27.54];
a_vals_haz = a0_haz:da_haz:af_haz;
KI_interp_haz = interp1(a_vector_KI_haz, KI_vector_haz, a_vals_haz,
 ↪  'spline', 'extrap');
N_haz = zeros(size(a_vals_haz));
for i = 2:length(a_vals_haz)
    KI = KI_interp_haz(i-1);
```

```
    dN = da_haz / (C_haz * KI^m_haz);
    N_haz(i) = N_haz(i-1) + dN;
end
N_haz = N_haz + N_tmaz(end);

N_total_m = [N_nz, N_tmaz, N_haz];
a_total_m = [a_vals_nz, a_vals_tmaz, a_vals_haz];


%% ================= m modified =================
% NZ
mm_nz = 3.8369;
N_nz_mm = zeros(size(a_vals_nz));
for i = 2:length(a_vals_nz)
    KI = KI_interp_nz(i-1);
    dN = da_nz / (C_nz * KI^mm_nz);
    N_nz_mm(i) = N_nz_mm(i-1) + dN;
end

% TMAZ
mm_tmaz = 3.5788;
N_tmaz_mm = zeros(size(a_vals_tmaz));
for i = 2:length(a_vals_tmaz)
    KI = KI_interp_tmaz(i-1);
    dN = da_tmaz / (C_tmaz * KI^mm_tmaz);
    N_tmaz_mm(i) = N_tmaz_mm(i-1) + dN;
end
N_tmaz_mm = N_tmaz_mm + N_nz_mm(end);

% HAZ
mm_haz = 3.5788;
N_haz_mm = zeros(size(a_vals_haz));
for i = 2:length(a_vals_haz)
    KI = KI_interp_haz(i-1);
    dN = da_haz / (C_haz * KI^mm_haz);
    N_haz_mm(i) = N_haz_mm(i-1) + dN;
end
N_haz_mm = N_haz_mm + N_tmaz_mm(end);

% Concatenar curva completa
N_total_mm = [N_nz_mm, N_tmaz_mm, N_haz_mm];
a_total_mm = [a_vals_nz, a_vals_tmaz, a_vals_haz];


%% ================= both curves =================
figure; hold on;
plot(N_total_m,  a_total_m,  'b--',  'LineWidth', 2);
```

```
plot(N_total_mm, a_total_mm, 'b', 'LineWidth', 2);

xlabel('Number of cycles, N');
ylabel('Crack length, a (mm)');
legend('m', 'm''', 'Location', 'NorthWest');
grid on;

%%%%%%%%%%%%%%%% ZONES %%%%%%%%%%%%%%%%

figure; hold on;
plot(N_nz_mm,   a_vals_nz,   'b-', 'LineWidth', 1.5);
plot(N_tmaz_mm, a_vals_tmaz, 'r-', 'LineWidth', 1.5);
plot(N_haz_mm,  a_vals_haz,  'g-', 'LineWidth', 1.5);

xlabel('Number of cycles, N');
ylabel('Crack length, a (mm)');
legend('NZ', 'TMAZ', 'HAZ', 'Location', 'NorthWest');
grid on;

xlim([0, 1.1*max(N_haz_mm)]);

```